J. Fluid Mech. (2001), *vol.* 440, *pp.* 235–268. Printed in the United Kingdom

On the rise of an ellipsoidal bubble in water: oscillatory paths and liquid-induced velocity

By KJETIL ELLINGSEN† AND FRÉDÉRIC RISSO‡

Institut de Mécanique des Fluides de Toulouse, UMR CNRS/INP-UPS 5502,
Allée du Professeur Camille Soula, 31400 Toulouse, France

(Received 18 May 2000 and in revised form 2 February 2001)

This work is an experimental study of the rise of an air bubble in still water. For the bubble diameter considered, path oscillations develop in the absence of shape oscillations and the effect of surfactants is shown to be negligible. Both the three-dimensional motion of the bubble and the velocity induced in the liquid are investigated. After the initial acceleration stage, the bubble shape remains constant and similar to an oblate ellipsoid with its symmetry axis parallel to the bubble-centre velocity, and with constant velocity magnitude. The bubble motion combines path oscillations with slow trajectory displacements. (These displacements, which consist of horizontal drift and rotation about a vertical axis, are shown to have no influence on the oscillations). The bubble dynamics involve two unstable modes which have the same frequency and are $\pi/2$ out of phase. The primary mode develops first, leading to a plane zigzag trajectory. The secondary mode then grows, causing the trajectory to progressively change into a circular helix. Liquid-velocity measurements are taken up to 150 radii behind the bubble. The nature of the liquid flow field is analysed from systematic comparisons with potential theory and direct numerical simulations. The flow is potential in front of the bubble and a long wake develops behind. The wake structure is controlled by two mechanisms: the development of a quasi-steady wake that spreads around the non-rectilinear bubble trajectory; and the wake instability that generates unsteady vortices at the bubble rear. The velocities induced by the wake vortices are small compared to the bubble velocity and, except in the near wake, the flow is controlled by the quasi-steady wake.

1. Introduction

Bubbly flows occur widely in both nature and industrial applications, including energy production (e.g. oil transportation, steam generators, cooling systems) and chemical engineering (e.g. bubbly columns, mixing in reactors, aeration systems). As a result, their significant practical importance has motivated numerous investigations during the past fifty years. However, despite this continuous effort, important questions remain open and thus the study of bubble behaviour remains an important field in fluid dynamics. The complexity is the result of the large number of interfaces that separate the gas and the liquid, two fluids having drastically different physical properties. In the first instance, this complicates theoretical and numerical approaches since each interface moves with its own velocity and may deform under the action of

---

† Present address: Norsk Hydro ASA, Research Centre Porsgrunn, PO Box 2560, N-3907 Porsgrunn, Norway.

‡ Author to whom correspondence should be addressed (e-mail: risso@imft.fr).

the liquid. Furthermore, the measuring techniques that are well suited for one phase are generally perturbed by the presence of the other phase.

The key problem in bubbly flows is to understand how the two phases interact. A general strategy may consist in distinguishing (i) the effect of the liquid on the bubbles, (ii) the effect of the bubbles on the liquid, and (iii) the role of the interactions between bubbles. In this context, knowledge of the behaviour of an isolated bubble is of major importance. It constitutes the reference situation for points (i) and (ii) in the absence of bubble interactions (iii). The reader is referred to Magnaudet & Eames (2000) for a recent review of the motions of an isolated bubble and to Risso (2000) for a general description of bubble deformations.

In the current study the focus is on the rise of a single bubble in a still liquid. Although this situation is elementary, it addresses numerous problems that are more general in application. The rise of a bubble is a complex problem since it involves interactions between the bubble deformation and the liquid flow field induced by the bubble motion. For pure fluids, it involves two independent non-dimensional numbers. Usually, one defines the Reynolds number ($Re = Vd/\nu$) which controls the flow regime around the bubble and the Weber number ($We = \rho V^2 d/\sigma$) which characterizes the bubble deformation (where ρ and ν are the liquid density and viscosity, σ is the interfacial tension, V is the bubble rise velocity). The bubble size is commonly defined by the equivalent diameter, d, which is the diameter of the sphere of the same volume (or by the equivalent radius, $R = d/2$). Let us consider the case of an air bubble rising in water. It is known that small bubbles remain spherical and their trajectory is rectilinear. Significant deformations appear for diameters larger than 1 mm, in which case the bubble takes on an ellipsoidal shape. Non-rectilinear trajectories are commonly observed for diameters ranging from 1.3 to 50 mm. Previous investigators (Saffman 1956; Aybers & Tapucu 1969*a*) have reported different kinds of trajectories: zigzag, helical path (also known as spiralling motion) and rocking motions. Obviously, the occurrence of these different motions will depend on the bubble diameter. However, they also depend on several complex mechanisms, including the action of surface-active contaminants, the coupling between path and shape oscillations, the initial conditions at the instant of bubble release and the presence of finite-amplitude perturbations. Although previous investigators have made a significant contribution, a general understanding of the problem is still lacking (see § 3.4 for a complete bibliography). First, the exact experimental conditions – especially the level of contamination – are often not precisely determined. In addition, the experimental techniques rarely provide a full description of the interface. Frequently, the following important issues are not addressed: Do the observed trajectories correspond to a transitory stage or to a stable final motion? Are shape oscillations present or not? What is the exact definition of zigzag and helical paths? The understanding of these oscillatory motions is however a key issue for bubbly flows, even when the motion of the continuous phase is turbulent. Indeed, it is only in microgravity condition that the path fluctuations of large bubbles ($1.5 \leqslant d \leqslant 50$ mm for air bubbles in water) are controlled by the turbulence (Risso 1999). In the normal gravity condition, the path oscillations related to the liquid mean drift velocity are robust and largely contribute to the bubble velocity fluctuations (Ford & Loth 1998). In most general situations, the prediction of bubble motions thus requires that these oscillations be taken into account.

The prediction of the velocity field induced by a moving bubble is another challenging problem (a complete bibliography is presented in § 4.1). Consider the liquid velocity at a fixed point in space. While a bubble is passing close to this point, liquid velocity fluctuations will be observed. An important point is the nature of such fluctuations. Even if the velocity field induced by the bubble is laminar and steady in the frame moving with the bubble, fluctuations are observed in the fixed laboratory frame. For oscillatory moving bubbles, the wake that develops behind the bubble is unsteady (Lunde & Perkins 1997; Brücker 1999) and may be turbulent. The liquid fluctuations are therefore due to different mechanisms of a different nature: steady wake, potential flow outside the wake, wake vortices that detach from the bubble rear and turbulence. Furthermore, these different phenomena produce a wide range of length scales ranging from less than one tenth the bubble radius in the near flow field up to several radii in the bubble wake. Hence the investigation of the liquid velocity fluctuations in bubbly flows requires that two problems are overcome: first the experimental techniques generally require the cutoff of a portion of the signal corresponding to measurements detected close to the bubble (see Suzanne *et al.* 1998); second, there are no established methods to distinguish between the different contributions to the measured liquid fluctuations. Knowledge of the flow field induced by a single bubble should allow the signal processing of the liquid velocity measurements and thus provide a basis for the interpretation of the liquid velocity fluctuations in general bubbly flows.

The objective of the present work is the description of the rise of a bubble in still water for well-defined experimental conditions. The bubble size ($d = 2.5$ mm, $Re = 8 \times 10^2$, $We = 3.6$) is chosen to correspond to the regime in which path oscillations are present but shape oscillations are not. It will be shown that the action of any surface-active contaminants can be regarded as negligible. At each instant, the full three-dimensional description of the interface is obtained by means of two high-speed video cameras and digital video processing. The liquid velocity is measured by a two-component laser Doppler anemometer, which is synchronized with the cameras. The experimental technique allows detection of all the length scales from 0.05 up 150 times R. The measurements of the liquid velocity will be compared with the predictions of the potential flow theory and the results of numerical simulations.

2. Experimental set-up

The experimental set-up is shown in figure 1. The test section was an open tank of 700 mm height with a squared cross-section of 150 mm width. To allow full optical access the four sides were of a glass construction. A stainless steel capillary tube (inside/outside diameter 0.33/0.50 mm) was located in the midpoint of the tank base. The tank was filled with tap water to a height of 650 mm above the capillary tip. Individual bubbles were formed by injecting air through the capillary with an air flow rate low enough ($< 160\,\mathrm{mm}^3\,\mathrm{s}^{-1}$) to ensure that the bubble volume at detachment was controlled by a static balance between the surface tension and buoyancy. Measurements, performed just after injection, confirmed that the bubble diameter remained constant, $d = 2.48 \pm 0.02$ mm. For the present experiments, the distance between two successive bubbles was always large enough to prevent interaction.

The bubble interface was filmed by means of a Kodak Ektapro EM high-speed video system at the rate of 1000 frames s^{-1}. To allow a three-dimensional description of the bubble behaviour, this system included the simultaneous use of two cameras. The first camera was set perpendicular to one side of the tank, directed in the y-direction. Floodlight 1 was located on the opposite side, facing camera 1. Owing to the space constraints, camera 2 had to be oriented with an oblique angle, α, to the tank side. Floodlight 2 faced the same tank side but with a symmetric orientation.

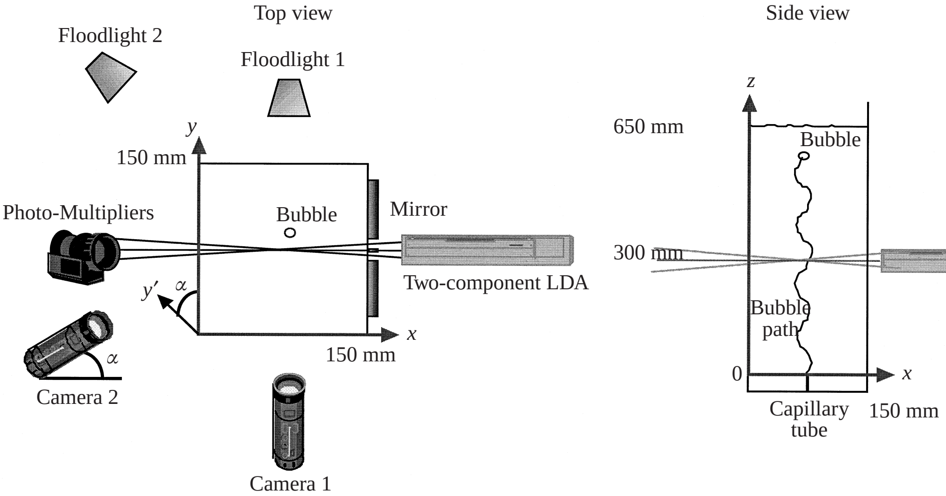

FIGURE 1. Experimental apparatus.

Set	Bubble equivalent diameter, d (mm)	Window width (mm)	Window elevation range (mm)	Pixel size (mm)	Angle of camera 2, $\alpha°$	LDA measuring volume (mm): Dimensions δx, δy, δz	LDA measuring volume (mm): Elevation	Number of runs
A	2.5	15	291.3–316.3	0.13	30	0.15, 0.04, 0.04	300	81
B	2.5	130	216.5–441.5 or 263.5–488.5	1.17	15	0.15, 0.04, 0.04	300	47

TABLE 1. Description of the experimental runs.

A mirror was used to reflect light, which then travelled through the bubble before reaching camera 2. Consequently, cameras 1 and 2 provided images of the bubble shadow onto the planes (x, z) and (y', z), respectively.

The number of pixels available to describe the images was 122 × 192 for camera 1 and 117 × 192 for camera 2. This resolution did not provide an accurate simultaneous description of both the bubble shape and its trajectory. For that reason, we performed two sets of experiments (see table 1). For set A, we used a small visualization window (25 mm height and 15 mm width), which permitted a high resolution: the pixel size was 0.13 mm. For set B, we chose a larger window, 130 mm wide and 225 mm high, which led to a pixel size of 1.17 mm. Together, the results provided by these two sets gave an accurate and complete description of the bubble shape, orientation and motion, for elevations ranging from 215 to 490 mm. Each experiment was commenced by recording the test region in the absence of a bubble and three images of the calibrated grid. After the runs, the images of the bubble interface were stored on videotape by means of an S-VHS VCR (Panasonic AG-7350).

The first step of video processing was to digitize each image using a Personal Computer equipped with a graphic A/D card (Imascan) and a frame synchronizer (GML PC TBC). The format of the digitized images is better than that of the camera:

740×574 pixels in 256 grey levels. Digitization was followed by the detection of the pixels that define the bubble contour. This step was achieved using in-house software based on classical image-processing algorithms: subtraction of the reference image without bubble, thresholding, binarization, dilatations and erosions. The complete procedure is described in detail by Ellingsen (1998) and is similar to that used by Risso & Fabre (1998). On obtaining the bubble contour, it is possible to determine the bubble projection seen by each camera. Measured lengths were converted from pixels to millimetres using the calibration images. The linear variation of the optical scale factor with the distance from the focal planes was corrected by an iterative procedure that used the information supplied by the two cameras (these corrections never exceeded 0.25%). Finally, the y-coordinate was determined by a rotation of angle α about the z-axis.

The overall accuracy depends on the experimental set that is considered. For both cases, the maximum error in the determination of the bubble contour was one pixel. For set A, the resulting accuracy of the bubble characteristics is, however, significantly better because of the larger number of pixels involved in their calculation. By assuming that the errors made in the determination of the different contour points are statistically independent, Ho (1983) provided an estimation of the standard deviation of the error made in the determination of the bubble centre. For experiments of set A, this theoretical estimation led to 0.05 pixel (0.007 mm). Tests using the calibration grids and comparisons between the measurements provided by the two cameras showed that the maximum errors were approximately seven times larger. Finally, we found that the accuracy of the bubble-centre coordinates, lengths of the minor and major axes and equivalent diameter was of ± 0.05 mm. Concerning the determination of the bubble-centre velocity, least-square fitting by equations (1) and (3) (see § 3.2) gave an accuracy of $\pm 0.1\,\mathrm{mm\,s^{-1}}$. For set B, it was only possible to determine the bubble centre. The accuracy of the raw data was ± 1 mm. However, by applying an appropriate linear filter it was possible to reduce the errors in the bubble-centre location and velocity to respectively ± 0.2 mm and $\pm 20\,\mathrm{mm\,s^{-1}}$.

In addition to bubble detection, a two-component laser Doppler anemometer (LDA) was used to measure the liquid velocity at a fixed point located at the tank centreline and 300 mm above the tip of the bubble injector. The LDA system consisted of an Ar-ion laser source (Spectra Physics 2020 ion) with a DANTEC optical arrangement that included two photo-multipliers equipped with green and blue filters, and two Burst Spectrum Analysers (DANTEC 57N25 & 57N10). The LDA provided measurements of the vertical component of the liquid velocity (z-direction) and one horizontal component (y-direction). The two measuring volumes were ellipsoids with a major axis of 0.15 mm in the x-direction, and two minor axes of 0.04 mm in the y- and z-directions. All LDA measurements were made in forward-scattering mode. However, owing to the small size of the measuring volumes, the data rate was small. We thus added a few decigrams of Iriodin 111 to the water contained in the tank. A comparison between experiments in the presence or absence of these tracers indicated no significant differences in the bubble shape or motion. The data rate after Iriodin addition ranged from 30 to 50 Hz. This is still low since the time taken by a bubble to travel a distance comparable to its own diameter is about 0.01 s. Because an experimental run was only interesting if a sufficient number of velocity samples were recorded, only 128 data sets from 5000 were retained for analysis. Our choice favoured the recordings where large velocities were detected. Consequently, regions of small velocities were not explored.

The accuracy of LDA measurements is not possible to estimate *a priori* (especially for samples detected close to the bubble). We avoided the detection of spurious samples by fixing the gain of the photo-multipliers to a low value and by removing measurements made when the LDA measuring volume intercepted the bubble. However, as shown in § 4.2, the ultimate validation of the experimental procedure is provided by the excellent matching between the measurements made close to the bubble front and the prediction provided by potential flow theory.

In summary, the experimental set-up described above provided time recordings of the two components of the liquid velocity when a rising bubble is passing close to a fixed point located 300 mm above the injection point. Since the clocks of the LDA and camera processors were synchronized, the location of the bubble interface relative to the LDA measuring volume was known at each instant. The accuracy in the interface detection was good enough to allow a description of all the scales that are present in the flow surrounding the bubble.

3. Dynamics of bubble motions

In this section the focus is on the interface behaviour. The following general trends are identified by visual inspection. When the bubble detaches from the injector, its shape is essentially spherical and it rapidly accelerates in the vertical direction. This first stage is followed by a period of reduced acceleration that leads to a less flattened bubble shape and the commencement of horizontal path oscillations. Beyond $z = 150$ mm the initial acceleration stage is achieved, the vertical velocity is approximately constant and the path-oscillation frequency is regular. The purpose of this work is to provide an accurate description of what happens during this period of regular oscillations. For this reason, all the measurements are performed in the region located between 215 and 490 mm above the injection point (see table 1). The presentation of the results will be separated into three parts. First, the bubble shape and orientation are described. This is followed by determination of the bubble trajectory characteristics and the manner in which these characteristics evolve with the elevation. Finally, the present results are compared with previous works and general conclusions are made.

3.1. *Bubble shape and orientation*

Experimental set A provided pairs of high-resolution images (figure 2*a*). This did not allow a direct determination of the bubble shape since only the projections on the two vertical planes (x, z) and (y', z) were available. Even if the bubble shape remains constant, the detected contours vary as the bubble orientation changes. In order to overcome this difficulty, we assume that (i) the bubble shape is an oblate ellipsoid of constant shape, and (ii) its axis of symmetry is parallel to the bubble-centre velocity. The bubble shape is thus totally defined by knowledge of its major axis (a) and its minor axis (b). The orientation is fully determined by the angle ϕ between the bubble velocity and the z-axis and the angle θ between the horizontal projection of the velocity and the x-axis. Under these conditions, the projected contours are ellipses. When $\phi = 0$ their major axis (a'), and minor axis (b') are respectively equal to a and b. Figure 2(*b*) compares the measured contour with an exact ellipse at an instant when $\phi = 0$. The comparison was repeated for the 81 runs of set A. In all cases the measured contour was similar to an ellipse with a major axis $a = 1.58 \pm 0.05$ mm and a minor axis $b = 0.77 \pm 0.05$ mm. The aspect ratio was $\beta = a/b = 2.05$ and the equivalent diameter $d = 2.49 \pm 0.05$ mm. This is in agreement with the diameter measured at

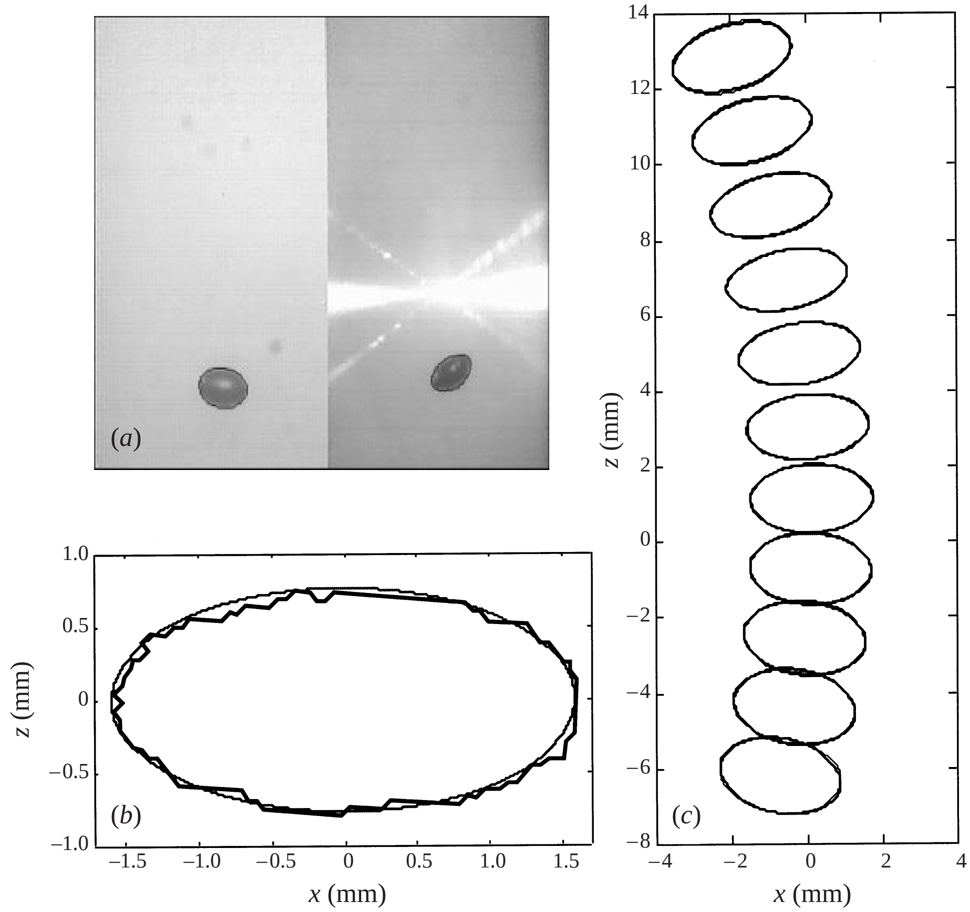

FIGURE 2. Bubble images and interface detection (—, detected contour; —, exact ellipsoid). (*a*) Images from the two cameras, (*b*) contour at the instant when the bubble rises vertically, (*c*) contours at different instants.

injection ($d = 2.48 \pm 0.02\,\mathrm{mm}$) since the effect of the reduction in hydraulic pressure was negligible for the range of elevations investigated.

The assumptions (i) and (ii) described above were validated at the instants when the bubble velocity is vertical. However it was necessary check them at other times. For each run, the projection in the plane (x, z) of an oblate ellipsoid (the symmetry axis of which is parallel to the measured bubble-centre velocity) is calculated. Figure 2(*c*) shows a comparison between the contour calculated using the assumptions (i) and (ii), and the measured contour. The excellent agreement indicated by this example is also exhibited by all the other experimental runs. Figure 3 shows the major and minor axes of the projected ellipsoid. Since the minor axis of the bubble is an axis of symmetry, the major axis of the ellipse is constant and equal to the major axis of the ellipsoid ($a' = a$). On the other hand, the minor axis of the ellipse varies in time and is larger than the minor axis of the ellipsoid ($b' \geqslant b$). Thus it is possible to confidently conclude that the bubble shape is similar to an oblate ellipsoid with an aspect ratio $\beta = a/b = 2.05$. After the initial acceleration stage, the shape remains constant and the bubble-centre velocity is parallel to the symmetry axis of the bubble.

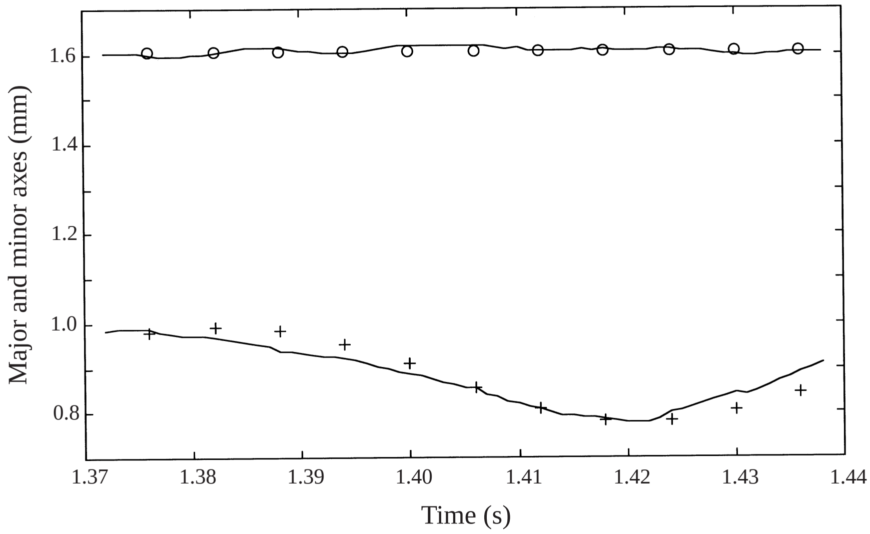

FIGURE 3. Time evolution of the principal axes of the bubble projection seen by camera 1. Measured values (——), major (○) and minor (+) axes calculated by assuming an exact ellipsoidal shape.

3.2. *Bubble motion close to* $z = 300\,mm$

The shape and orientation of the bubble being known, a complete description of the interface requires the determination of the motion of the bubble centre. Using the results of set A, the bubble motion in the region near 300 mm above the injection point is first investigated ($291.3 \leqslant z \leqslant 316.3$ mm). Figures 4–6 show three examples of bubble motion recordings. Since the amplitude of vertical oscillations is weak, the effect of the mean vertical velocity (which is $\langle V_z \rangle = 309\,\text{mm}\,\text{s}^{-1}$ for all runs) has been subtracted in the representation of the vertical coordinate (figures 4–6*a*). These recordings clearly indicate the existence of oscillations in both the horizontal and vertical directions. The frequency of the vertical oscillations is larger than that of the horizontal oscillations whilst the amplitude is significantly smaller. Unfortunately, these recordings are shorter than one complete period of oscillation and so the following method was developed to accurately determine the oscillation characteristics. For each recording, we assume that the horizontal coordinates may be written:

$$x(t) = l_x \sin(\omega(t - t_{x0})) + x_0, \quad y(t) = l_y \sin(\omega(t - t_{y0})) + y_0, \tag{1}$$

where t is the time. The angular frequency ω, the amplitudes l_x and l_y, the time origins t_{x0} and t_{y0} and the spatial origins x_0 and y_0 were determined for each run by least-square fitting of the experimental results. This procedure showed that the angular frequency was the same for all the 81 runs: $\omega = 39\,\text{rad}\,\text{s}^{-1}$. This value will be confirmed in § 3.3 from the longer duration recordings represented by set B. Therefore it was considered appropriate to impose this value for the determination of the other parameters. The corresponding fitted results are in agreement with the measurements (figures 4–6*b*, *c*).

Equation (1) is of interest from a signal-processing point of view. By eliminating the noise due to the finite pixel size, it allows an accurate determination of the bubble velocity. In addition it allows interpolation of the signals in the region where bubble detection is prevented by the presence of the laser beams. However (1) is also of

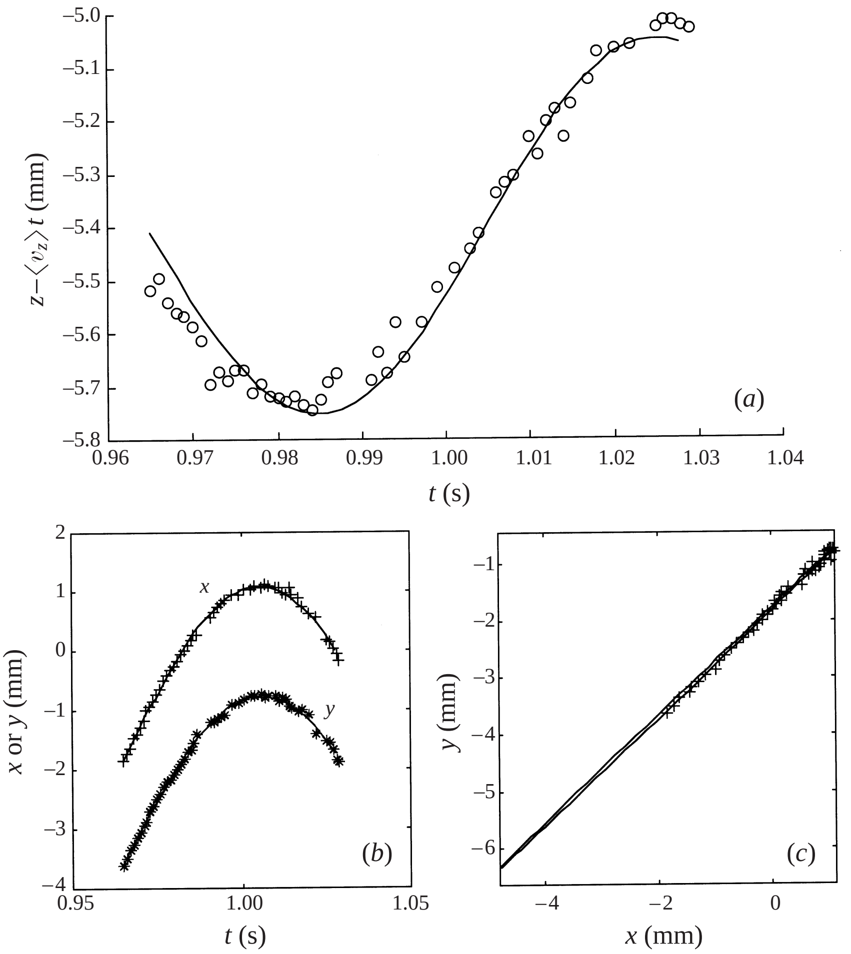

FIGURE 4. Time evolution of the bubble-centre coordinates: example of plane trajectory from set A. (*a*) Vertical coordinates, (*b*) horizontal coordinates, (*c*) projection of the trajectory on a horizontal plane: symbols represent measurements, lines correspond to least-square fitting (equations (1) and (3)).

interest in a broader sense. The horizontal projection of the trajectory is an ellipse, the major axis of which is the same for all the runs. This suggests that it is possible to apply to each trajectory a rotation about a vertical axis to ensure coincidence of the major axis of each ellipse. The rotation angle is determined analytically from the parameters l_x, l_y, t_{x0}, t_{y0} that were previously estimated by least-square fitting. In this principal frame (ξ', η'), (1) becomes

$$\xi'(t) = L_\xi \sin(\omega(t-\tau)) + \xi_0, \quad \eta'(t) = \varepsilon L_\eta \cos(\omega(t-\tau)) + \eta_0. \tag{2}$$

In this way the amplitude of the principal oscillation is the same for all the runs ($L_\xi = 4.3$ mm). The frequency ω is still equal to 39 rad s^{-1} and ε to $+1$ or -1 depending on which direction the bubble moves on the ellipse. The only remaining adjustable parameters are the amplitude of the secondary oscillations, L_η, the time origin, τ, and the coordinates of the ellipse centre, ξ_0 and η_0. They are again determined by least-square fitting of the experimental bubble coordinates which were previously expressed in the principal frame.

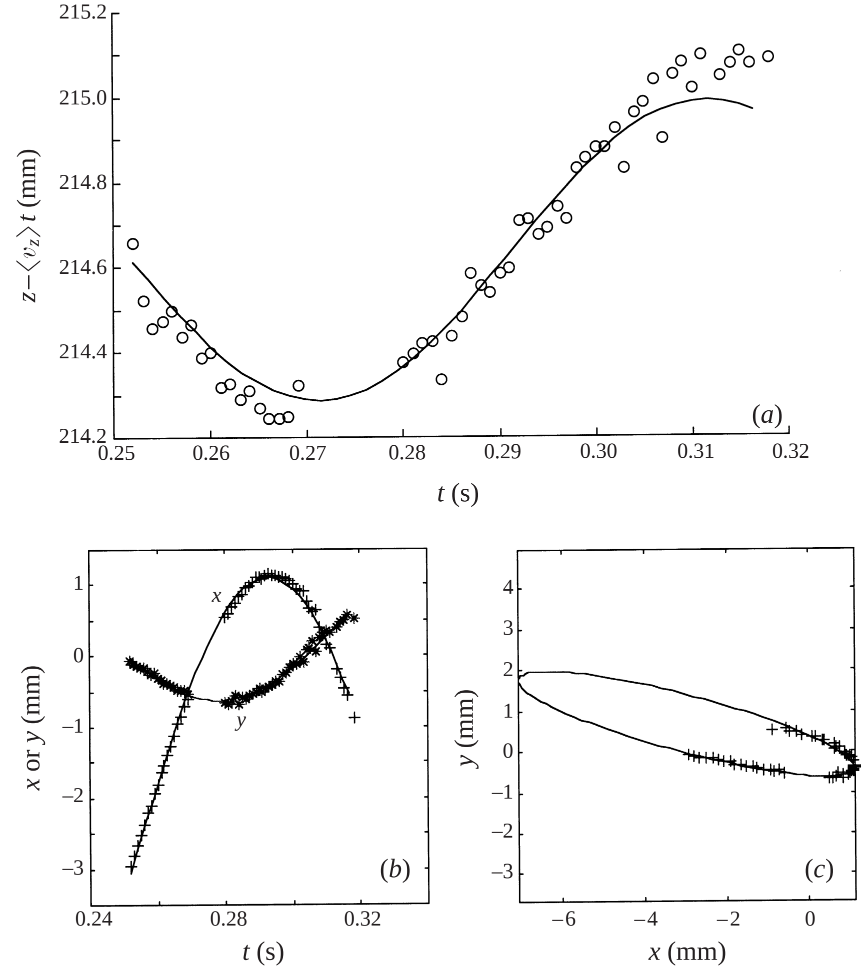

FIGURE 5. As figure 4 but showing an example of flat helical path from set A.

From the comparison of ξ' and z, it is clear that the frequency of the vertical oscillations is twice that of the horizontal ones and that the phase difference between oscillations in the z- and ξ'-directions is equal to π. The vertical bubble coordinate may hence be written

$$z(t) = L_z \sin(2\omega(t-\tau)) + \langle v_z \rangle t + z_0. \tag{3}$$

The amplitude of these weak oscillations, $L_z = 0.35 \pm 0.05$ mm, and the mean rise velocity, $\langle v_z \rangle$, are independent of the run being considered. The time origin τ having been determined from the horizontal components, the only adjustable parameter is the vertical origin z_0, which is again determined by least-square fitting. The comparison between the (3) and the experimental results is presented in figures 4–6*a*.

It is now possible to compare the trajectories for the different runs. In addition to the rotation, we apply to the measurements the translation defined by: $\xi = \xi' - \xi_0$, $\eta = \eta' - \eta_0$, $\zeta = z - z_0$ (see figure 7). Figure 8 presents the results of 71 different runs in the principal frame (ξ, η, ζ). The projections of all the trajectories on the plane of primary oscillations (ξ, ζ) coincide closely. The secondary oscillations – plane

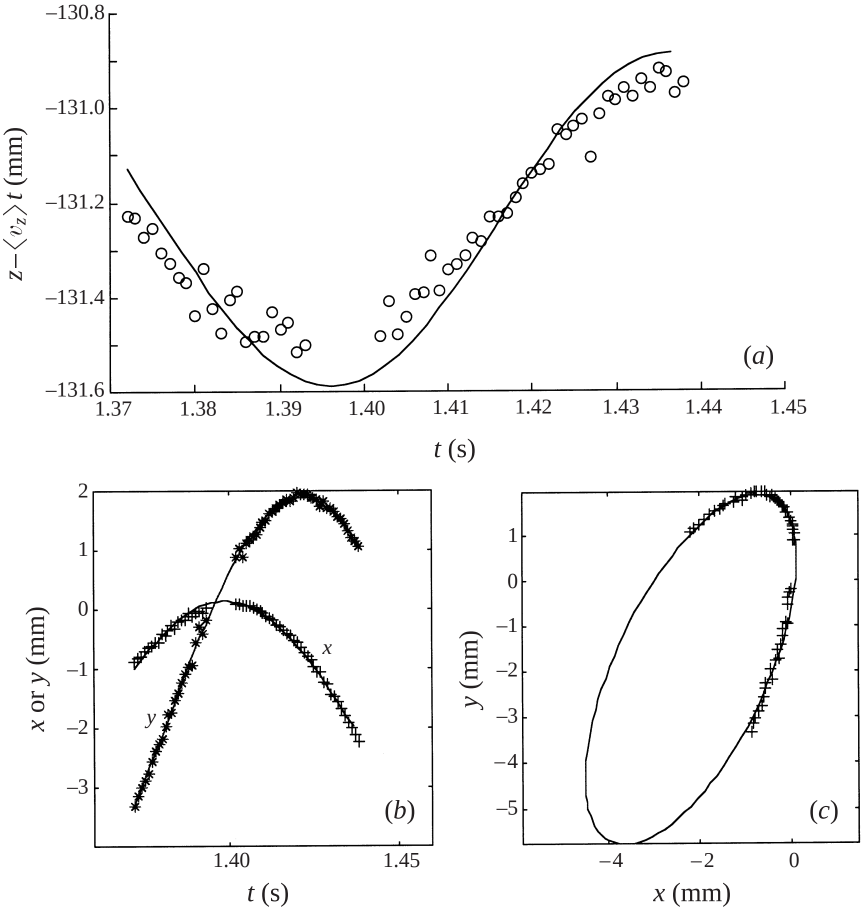

FIGURE 6. As figure 4 but showing an example of helical path from set A.

(η, ζ)−are $\pi/2$ out of phase relative to the primary oscillations. Their amplitude, L_η, varies from one run to the next. In most cases, L_η is small compared to L_ξ. For 40% of the occurrences L_η is less than $0.06L_\xi$ and for 90% less than $0.23L_\xi$. In addition, the maximum value of L_η observed is $0.6L_\xi$. The trajectories are thus quite similar to plane zigzags but can more generally be described by flattened helixes. Finally, after a displacement (translation and vertical rotation) and a change of time origin the motion of all the observed bubbles may be described within the limit of experimental errors (± 0.05 mm) by the following equations:

$$\xi(t) = L_\xi \sin(\omega t), \tag{4}$$

$$\eta(t) = \varepsilon L_\eta \cos(\omega t), \tag{5}$$

$$\zeta(t) = L_\zeta \sin(2\omega t + \pi) + \langle v_\zeta \rangle t, \tag{6}$$

where $\omega = 39\,\mathrm{rad\,s^{-1}}$, $L_\xi = 4.3\,\mathrm{mm}$, $L_\zeta = L_z = 0.35\,\mathrm{mm}$, $\langle v_\zeta \rangle = \langle v_z \rangle = 309\,\mathrm{mm\,s^{-1}}$, $\varepsilon = \pm 1$, and $L_\eta < L_\xi$. The bubble motion is now fully characterized in a small region centred 300 mm above the injection point. This motion is characterized by two modes of horizontal oscillations with the same frequency, in two perpendicular directions and with a phase difference of $\pi/2$. The amplitude of the primary mode

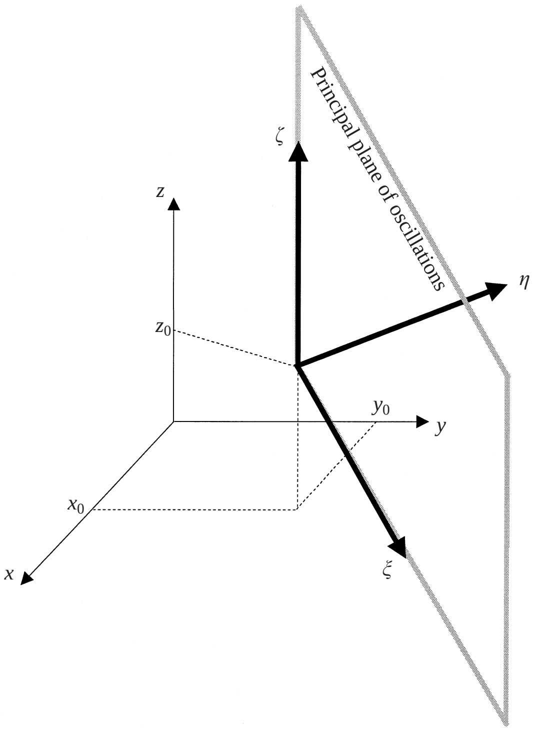

FIGURE 7. Definition of the principal frame of oscillations (ξ, η, ζ).

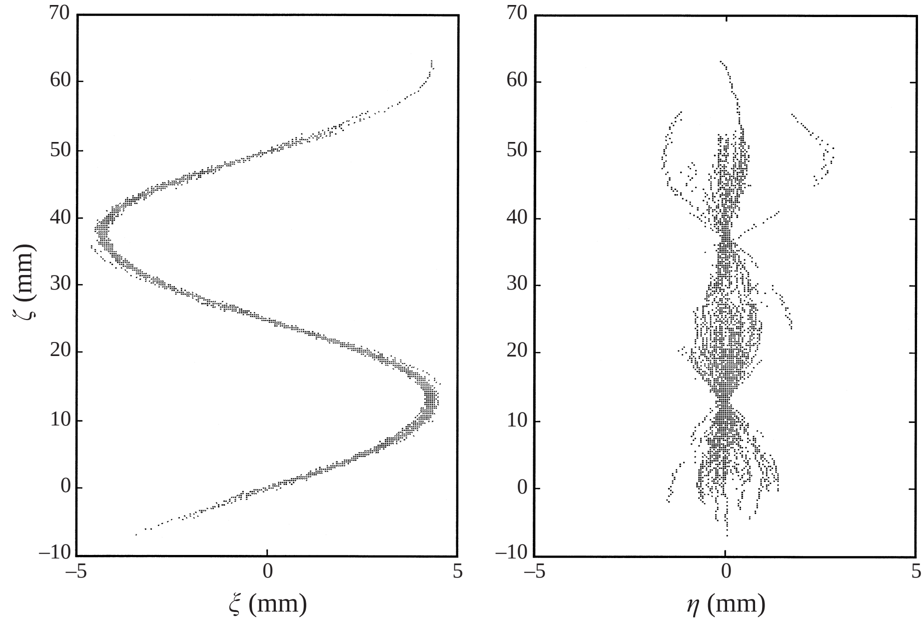

FIGURE 8. Superimposition of 71 bubble trajectories in the principal frame of oscillation.

is determined while that of the secondary one depends on the experimental runs. The vertical motion shows weak oscillations at twice the frequency of the horizontal motion. Their amplitude, their phase and the mean rise velocity are determined.

At this point, we propose the following interpretation. The rectilinear trajectory is

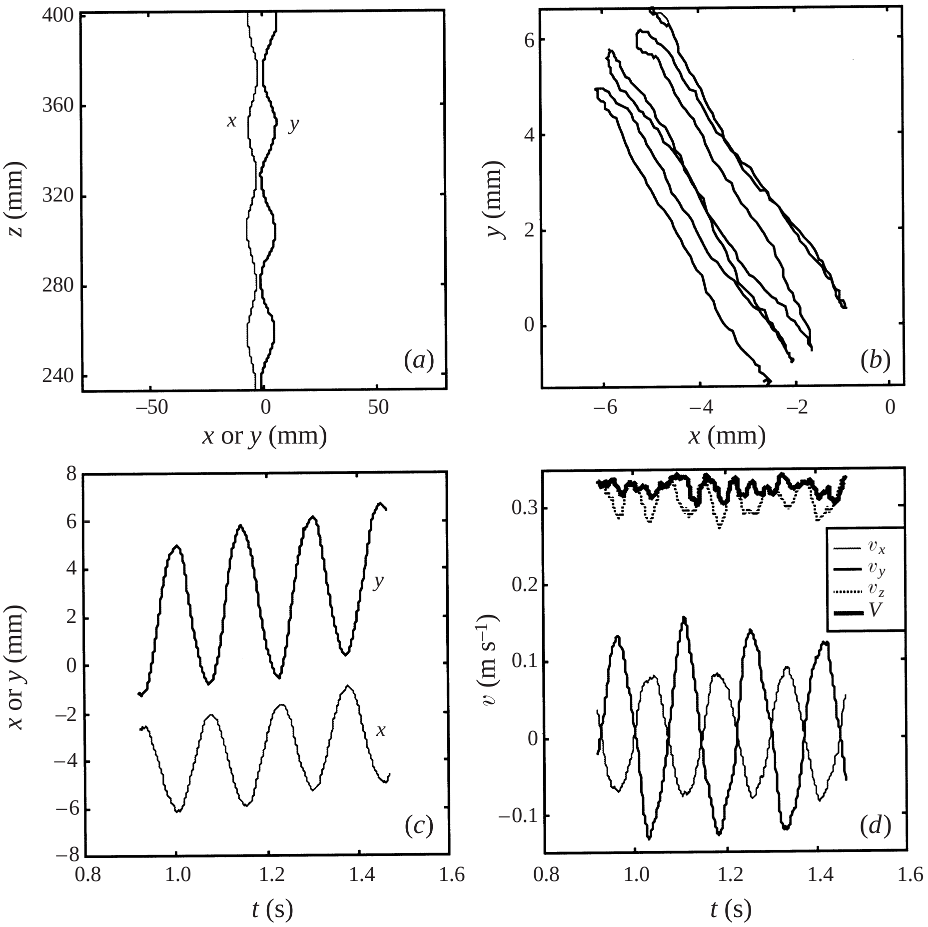

FIGURE 9. Bubble-centre coordinates and velocity in the laboratory frame: case 1 from set B. (*a*) Vertical projections of the trajectory, (*b*) horizontal projection of the trajectory, (*c*) time evolution of the horizontal coordinates, (*d*) time evolution of the velocity components and magnitude.

unstable. The initial conditions correspond to the detachment of a bubble from the tip of the injector in a tank filled with water at rest. However, as is to be expected in any experiments, small initial perturbations are present, owing to which plane oscillations develop and the trajectory becomes a plane zigzag. The phase and direction of the oscillations are random, indicating that the initial perturbations are random also. At 300 mm above the injection point, the amplitude of the first unstable mode is saturated and independent of the initial perturbations. However, the plane zigzag is also unstable and a second mode of oscillations develops. Its amplitude is not yet saturated and still depends on the initial perturbations. Finally, it is worth noting that for strong initial perturbations (Saffman 1956), it is possible to observe a helical motion without first observing the transitory zigzag motion.

3.3. *Evolution of the bubble motion with height*

Having characterized the bubble motion in the region 300 mm above the injection point by equations (4)–(6), the objective becomes to determine whether this motion

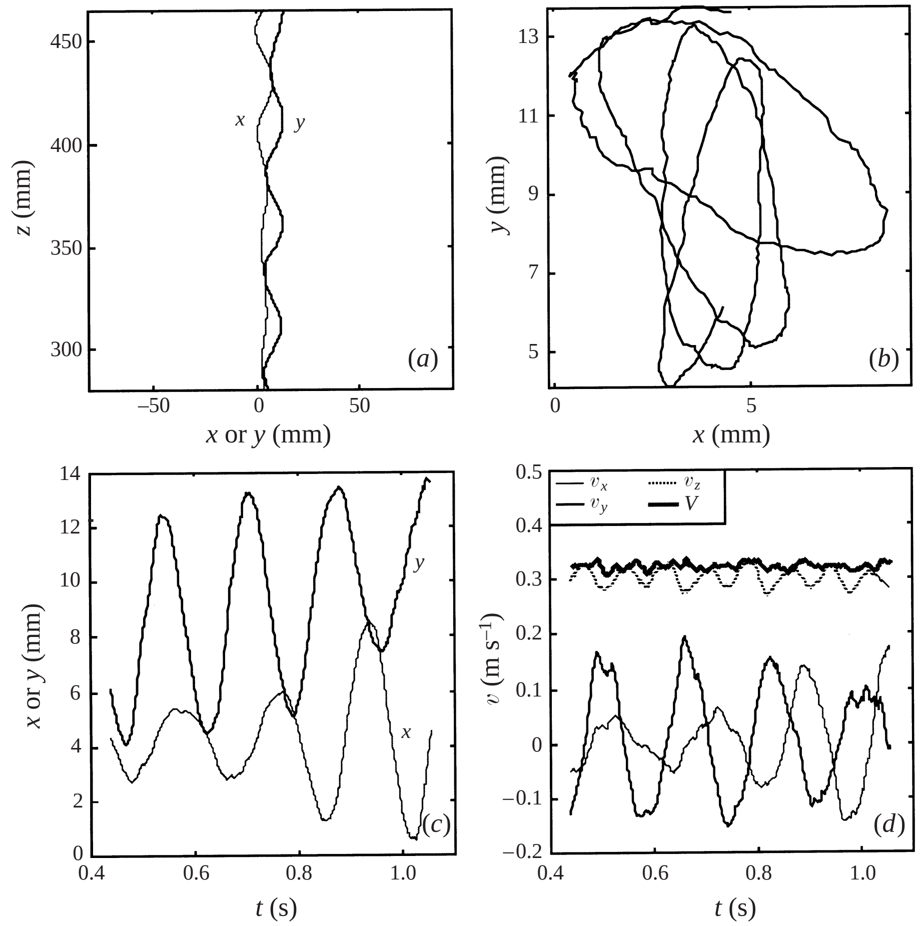

FIGURE 10. As figure 9 but for case 2 from set B.

evolves with height. In particular, we intend to use the results of set B to determine how the parameters ω, L_ξ, L_ζ and $\langle v_\zeta \rangle$ change with height.

Figures 9 and 10 show the results of two different runs (hereafter referred to case 1 and 2). Let us consider first case 1. The evolution of x and y versus z (figure 9*a*) or time (figure 9*c*) show regular oscillations with a wavelength close to 50 mm and an angular frequency of 39 rad s^{-1}. This is in agreement with the results obtained near $z = 300$ mm. However, the projection of the trajectory onto the horizontal plane (figure 9*b*) is neither a straight line nor an ellipse and is thus not compatible with equations (4) and (5). Inspection of the time evolution of the velocity (figure 9*d*) shows that the only difference with (4) and (5) is the existence of an additional constant drift velocity. By removing this velocity from the measurements, a plane zigzag motion is obtained. Since the evolution of x and y are half a period out of phase, the principal directions of oscillations are obtained by a rotation of 45° about the vertical axis. Case 2 (figure 10) is more complex. A constant drift is observed in the y-direction. However figure 10(*b*) shows that the principal directions of oscillations are also continuously changing. In order to obtain a motion compatible with (4) and (5), it would be necessary to apply a rotation about a vertical axis, the angle of which continuously changes with the elevation z.

All the experimental runs belonging to set B confirm the above trends. The wavelength and the frequency of the oscillations remain unchanged the latter will be ascertained by the analysis in the principal frame of oscillations. Sometimes, the trajectory is a plane zigzag or a flattened helix compatible with (4) and (5). At other times, the motion is the same except for the presence of an additional horizontal constant drift. It is also possible to observe times for which is no mean drift, but the principal axes of oscillations rotate during the motion. Finally, we also observe combinations of a velocity drift and a continuous rotation. These rotation and drift effects are not reproducible. It is hence not possible to describe them from a deterministic point of view. Thus, it was considered appropriate to try to remove these effects from the experimental results.

Consider the horizontal components of the bubble velocity, $v_x(t)$ and $v_y(t)$. The removal of the constant drift is achieved by subtracting the average velocity of each recording: we thus obtain the centred signals $v'_x(t)$ and $v'_y(t)$. Removing the rotation effect is more complex. The results of § 3.2 showed that, for a short duration, $v'_x(t)$ and $v'_y(t)$ are harmonic functions. This suggests that they are harmonic functions with amplitudes that slowly vary in time:

$$v'_x(t) = l_{vx}(t) \sin(\phi_x(t)), \quad v'_y(t) = l_{vy}(t) \sin(\phi_y(t)). \tag{7}$$

This decomposition can be achieved from the Hilbert transform (Melville 1983) HF, of the signal $v'_x(t)$, obtained from the Fourier transform, FT:

$$\mathrm{HF}\,[v'_x(t)] = \mathrm{FT}^{-1}[-\mathrm{i}\,\mathrm{sgn}(f)\mathrm{FT}\,[v'_x(t)](f)]. \tag{8}$$

The amplitude and the phase are then given by

$$l_{vx}(t) = |v'_x(t) + \mathrm{iHF}\,[v'_x(t)]|, \quad \phi_x(t) = \mathrm{Arg}\,\{v'_x(t) + \mathrm{iHF}\,[v'_x(t)]\}. \tag{9}$$

The determination of $l_{vy}(t)$ and $\phi_y(t)$ is similarly obtained from the Hilbert transform of $v'_y(t)$. Knowledge of the instantaneous amplitudes, l_{vx} and l_{vy}, and phase differences, $\phi_x - \phi_y$, allows the determination of the instantaneous principal directions of oscillations. Then, by applying a rotation, the principal amplitudes of oscillations, $L_{v\xi}$ and $L_{v\eta}$, are obtained. Figures 11 and 12 present the results of this treatment for cases 1 and 2.

Initially the focus is on case 1. Figure 11(*a*) shows the instantaneous amplitudes, l_{vx} and l_{vy}, of the velocity oscillations visible in figure 9(*d*). The time derivatives of ϕ_x and ϕ_y (figure 11*b*) are the angular frequency of these oscillations. Since $\phi_x(t)$ and $\phi_y(t)$ are two straight lines with the same gradient, the oscillation frequencies of v_x and v_y are equal and constant (39 rad s^{-1}). In the principal frame (figure 11*c*), the amplitude of the primary mode is constant ($L_{v\xi} = 0.15\,\mathrm{m\,s^{-1}}$) (the residual variations are smaller than the measurement accuracy, which is $\pm 20\,\mathrm{mm\,s^{-1}}$) and the amplitude of the secondary mode is negligible: the motion is thus similar to a plane zigzag. This is clearly illustrated by the comparison of figures 9(*b*) and 11(*d*). After rotation and drift removal, the projection on the horizontal plane becomes a horizontal straight line. Next case 2 is considered (figure 12). In the laboratory frame, the evolution of the amplitude is complex (figure 12*a*). However in the principal frame, the amplitude of the primary mode is constant ($L_{v\xi} = 0.16\,\mathrm{m\,s^{-1}}$) and that of the secondary mode increases in a regular way. After rotation and drift removal, the trajectory is thus similar to a flattened helix that progressively becomes less and less flattened. The projection on the horizontal plane (figure 12*d*) is an ellipse, the major axis of which is constant while the minor axis is continuously increasing.

The same treatment applied to all the runs of set B leads to the following general

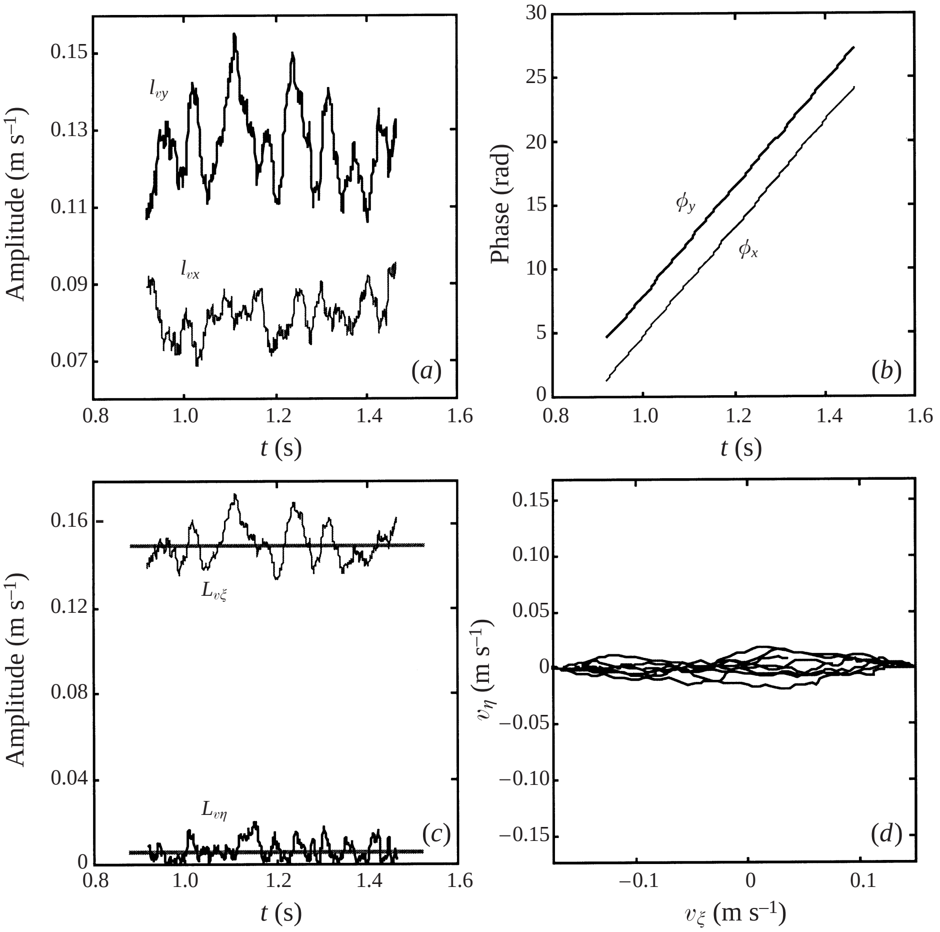

FIGURE 11. Bubble-centre velocity: case 1 from set B. (*a*) Amplitudes and (*b*) phases of the two modes of oscillations in the laboratory frame, (*c*) principal amplitudes of the two modes, (*d*) horizontal velocity in the principal frame of oscillation.

conclusions. The frequencies of the two modes are equal and constant ($\omega = 39.4 \pm 1\,\mathrm{rad\,s^{-1}}$) and the amplitude of the primary mode is constant ($L_{v\xi} = 0.16 \pm 0.02\,\mathrm{m\,s^{-1}}$). Concerning the amplitude of the secondary mode, two different situations may be distinguished. The first one corresponds to case 1: $L_{v\eta}$ is negligible and remains so during the whole recording duration. The second is analogous to case 2: $L_{v\eta}$ continuously increases during the duration of observation. After rotation and drift removal, the horizontal oscillations thus still obey equations (4) and (5). Concerning vertical oscillations, the results show that the velocity magnitude, V, is constant for all the considered runs and elevations:

$$V = (v_\xi^2 + v_\eta^2 + v_\zeta^2)^{1/2} = 0.325 \pm 0.02\,\mathrm{m\,s^{-1}}. \tag{10}$$

By taking of derivative of (4) and (5) and combining with (10) one finds

$$v_\zeta(t) = V\{1 - (\omega L_\xi / V)^2 \cos^2 \omega t - (\omega L_\eta / V)^2 \sin^2 \omega t\}^{1/2}. \tag{11}$$

By assuming that the trajectory is a plane zigzag ($L_\eta = 0$) and that the oscillations

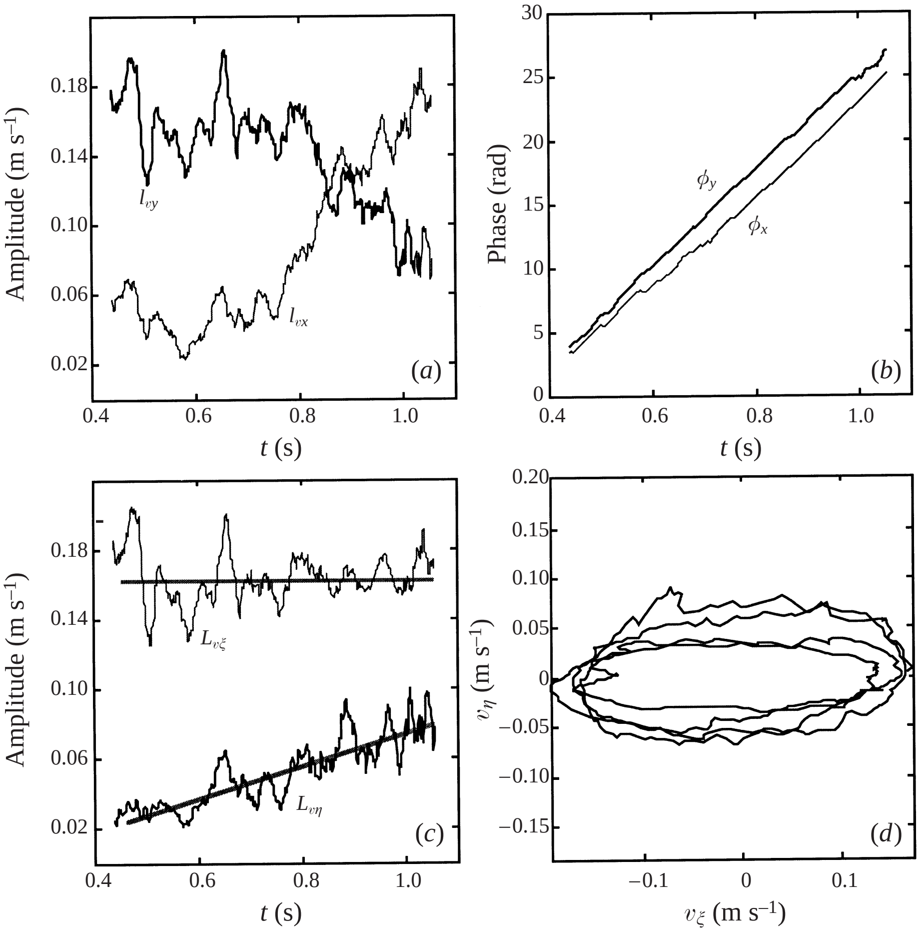

FIGURE 12. As figure 11 but case 2 from set B.

are small compared to the velocity magnitude ($\omega L_\xi/V \ll 1$), integration of (11) yields

$$\zeta(t) = \{1 - \tfrac{1}{4}(\omega L_\xi/V)^2\}Vt + (\tfrac{1}{8}\omega L_\xi^2/V)\sin(2\omega t + \pi) + O(\{\omega L_\xi/V\}^3). \tag{12}$$

In the limit of measurement accuracy, the values of $\langle V_\zeta \rangle$ and L_ζ in (6) are equal to the coefficients of t and $\sin(2\omega t + \pi)$ in (12). Equation (6) may be considered to be an approximation of (10) for plane zigzag motions. The weak oscillations that were observed in the vertical direction seem to be driven by the horizontal oscillations under the constraint imposed by a constant velocity magnitude. Now, by assuming that the trajectory is a circular helix ($L_\xi = L_\eta = L$), the following relation is found:

$$\zeta(t) = \{1 - \tfrac{1}{2}(\omega L/V)^2\}Vt. \tag{13}$$

This suggests that, when the amplitude of the secondary mode is equal to that of the primary mode, the vertical velocity will reach a constant value. One may also expect that the mean vertical velocity should decrease as the amplitude of the secondary mode increases.

In the principal frame of oscillations, the velocity of the bubbles may finally be described by

$$v_\xi(t) = L_{v\xi}\cos(\omega t), \tag{14}$$

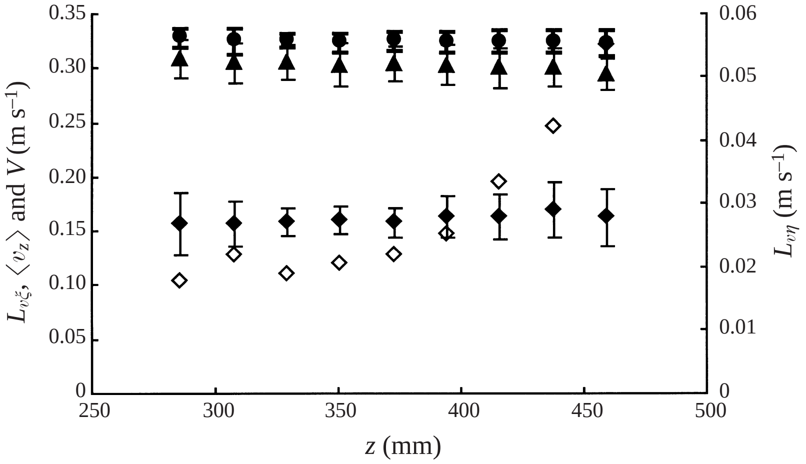

FIGURE 13. Evolution of the bubble-motion characteristics with the elevation: •, V; ▲, $\langle v_z \rangle$; ◆, $L_{v\xi}$; ◇, $L_{v\eta}$. Each point is determined by averaging the 47 runs of set B (for clarity, errors bars are not shown for $L_{v\eta}$ since it varies from 0 to 0.7 between the different runs).

$$v_\eta(t) = \varepsilon L_{v\eta} \sin(\omega t). \tag{15}$$

$$v_\zeta(t) = (V^2 - V_\xi^2 - V_\eta^2)^{1/2}. \tag{16}$$

Figure 13 presents the spatial evolution of the trajectory characteristics. They are determined for each elevation by averaging over the 47 runs of set B. The amplitude $L_{v\xi}$ (0.16 ± 0.01 m s^{-1}) and the velocity V(0.325 ± 0.005 m s^{-1}) do not evolve with z. The growth of the secondary mode, $L_{v\eta}$, is clearly visible since its average value increases from 0.02 to 0.055 m s^{-1} when z increases from 290 to 460 mm. A slight decrease of the mean vertical velocity $\langle v_z \rangle$ is also observed, from 0.31 to 0.29 m s^{-1}. This can be attributed to the observation that the velocity magnitude remains constant whilst the amplitude of the horizontal oscillations increases.

The interpretation proposed at the end of § 3.2 is thus confirmed. After the initial acceleration stage, the velocity magnitude reaches an almost constant value. Oscillations develop in a horizontal direction. The amplitude of this primary unstable mode is saturated at 300 mm above the injection point. A second unstable mode is also frequently observed. It is characterized by oscillations in the perpendicular horizontal direction, at the same frequency and $\pi/2$ out of phase relative to the primary mode. The amplitude of the second mode at $z = 300$ mm is weak and depends on the run considered but increases with the elevation. Importantly, it never reached its saturated value within the region under investigation ($z \leqslant 490$ mm). The existence of these two modes should lead to the observation of an initial rectilinear path, which first changes into a plane zigzag as the primary mode grows and then transforms into a helix as the second mode develops. The actual paths are however more complex owing to the existence of a weak drift of the trajectory centre and a slow rotation of the principal directions of oscillations. This drift and rotation is not reproducible. However, since they are shown to have no influence on the oscillations, it is legitimate to analyse the motion in the principal frame of oscillations.

3.4. *Comparison with other studies and discussion*

The present work focuses on air bubbles rising in still water. Their equivalent diameter is $d = 2.5$ mm. The measured velocity magnitude is $V = 0.325$ m s^{-1}. This corresponds to a Reynolds number, $Re = Vd/\nu$, of 8×10^2, and a Weber number, $We = \rho V^2 d/\sigma$, of 3.6. Having analysed the motion of bubbles under these conditions it is appropriate to make comparisons with previous results available in the literature.

Moore (1965), El Sawi (1974) and Miskis, Vanden-Broeck & Keller (1981) have proposed theoretical predictions of the bubble shape based on the potential flow theory. Their studies all lead to the same conclusion that for Weber numbers greater than approximately 3.2 no axisymmetric steady solution exists. This is in contrast with the present experiments where a steady axisymmetric shape for $We = 3.6$ was clearly observed. Moreover, Miskis *et al.* (1981) predicted a Weber number of 2.8 for the bubble aspect ratio observed here. Ryskin & Leal (1984) and Blanco (1995) performed direct numerical simulations of axisymmetric deformable bubbles. No simulations are available for the present parameters. Ryskin & Leal found aspect ratios of $\beta = 1.5$ for ($Re = 2 \times 10^2$, $We = 3$) and $\beta = 1.85$ for ($Re = 2 \times 10^2$, $We = 4$). Blanco obtained $\beta = 1.85$ for ($Re = 3.8 \times 10^2$, $We = 3.4$). Although these results are not directly comparable to the results presented here, they clearly demonstrate that axisymmetric shapes exist for Weber numbers greater than 3.2. This conclusion is confirmed by the experimental investigations of Aybers & Tapucu (1969*a*) and Duineveld (1994, 1995).

In two companion papers, Aybers & Tapucu (1969*a*, *b*) performed an extensive experimental investigation of air bubbles rising in water for $0.8 \leqslant d \leqslant 4$ mm. The bubble shape was determined from photographs. Since images were taken in one plane only, the authors could not determine the bubble aspect ratio for any bubble orientation. Consequently the photographs were taken close to the injection point ($0 \leqslant z \leqslant 40$ mm), during the initial accelerating stage where the bubble motion was rectilinear. They presented the measured aspect ratio versus both the bubble diameter and the Weber number. For the same diameter as the present study ($d = 2.5$ mm), Aybers & Tapucu (1969*b*) find a larger deformation ($\beta = 2.5$) than that found here. This difference is due to the fact that the maximal bubble velocity during the initial rectilinear stage is greater than the terminal velocity reached on oscillating paths. For the same Weber number ($We = 3.6$), they however find the same aspect ratio as that reported here. More recently, Duineveld (1995) investigated the rise of air bubbles in ultra-purified water by means of a high-speed video camera. The study is limited to rectilinear rising bubbles since the diameters under consideration varied from 1 to 2 mm. In this range, Duineveld finds that the aspect ratio is an increasing function of the diameter (the value $\beta = 2$ is reached at $d = 2$ mm). Using the fitting proposed by Duineveld to extrapolate the results for greater diameters, it is found that $\beta = 2.8$ for $d = 2.5$ mm. This is not in contradiction with the present result. The rise velocity is an increasing function of the diameter up to $d = 1.8$ mm where it reaches a maximum and then decreases. Consequently there exists a diameter close to 2 mm beyond which the Weber number starts to decrease also. As the deformation remains an increasing function of the Weber number, the aspect ratio becomes a decreasing function of the bubble diameter. The relationship proposed by Duineveld between the aspect ratio and the Weber number leads to $We = 3.4$ for $\beta = 2.05$, which is similar to the current result.

Concerning the bubble orientation, Saffman (1956) was the first to assume that, during path oscillations, the revolution axis of the bubble is at each instant parallel to the bubble-centre velocity. This was experimentally observed by Duineveld (1994) and Lunde & Perkins (1998). From full three-dimensional interface detection, the present work provides a definitive confirmation of this point.

The comparisons with the different results available seem to indicate that the relationship between the Weber number and the aspect ratio is independent of the motion type (i.e. rectilinear at constant speed, rectilinear accelerated or oscillating paths). The fact that the velocity magnitude and orientation remains constant after the initial acceleration stage seems to explain the observation that the bubble shape remains fixed during zigzag and helical path oscillations. Of course, this result does not hold for large bubbles for which the Weber number is again an increasing function of the diameter. Indeed, for large Weber numbers the surface tension cannot maintain a constant bubble form and so shape oscillations appear. Duineveld (1995) experimentally determined that the onset of shape oscillations occurs at $We = 4.2$. Later, Lunde & Perkins (1998) observed shape oscillations for $d = 3.52$, 4.32 and 5.16 mm and analysed their coupling with path oscillations.

Path oscillations have been investigated by numerous experimenters including Haberman & Morton (1954), Saffman (1956), Hartunians & Sears (1957), Aybers & Tapucu (1969*a,b*), Mercier, Lyrio & Forslund (1973), Tsuge & Hibino (1977), Duineveld (1994, 1995), Lunde & Perkins (1997, 1998), Ellingsen & Risso (1998) and Ford & Loth (1998). Different regimes exist depending on the equivalent bubble diameter. Small bubbles and large spherical caps rise on a straight line. Between these two limits, bubbles of intermediate size perform path oscillations. For air bubbles in tap water, Aybers & Tapucu (1969*a*) reported the following: rectilinear motion for $0 \leqslant d \leqslant 1.34$ mm, helical motion for $1.34 \leqslant d \leqslant 2$ mm, plane zigzag changing into helical path for $2.00 \leqslant d \leqslant 3.60$ mm, plane zigzag for $3.60 \leqslant d \leqslant 4.20$ mm and rocking motion for $d > 4.20$ mm. These general trends qualitatively agree with other works. Nevertheless, the occurrence of zigzag and helical paths has been shown to depend either on initial conditions or small perturbations (Saffman 1956; Lunde & Perkins 1997). In some circumstances a perturbed zigzag may transform into a helix, although the reverse has never been observed. Furthermore, the onset of the different regimes depends on the presence of surface-active contaminants (Hartunians & Sears 1957; Tsuge & Hibino 1977; Aybers & Tapucu 1969*a*; Bel Fdhlia & Duineveld 1996). Using ultra-purified water, Duineveld (1995) showed that path oscillations start for a diameter significantly greater than that determined by Aybers & Tapucu (1969*a*): $d = 1.82$ mm ($We = 3.3$, $Re = 660$). Since tap water was used in the current study, it is necessary to determine whether the results of the present work are influenced by the presence of surface-active contaminants. As the bubble moves, the surfactants deposit on the surface and are swept from the front to the rear. This means that the contaminants tend to accumulate at the rear of the bubble as the velocity increases. By adding well-defined quantities of surfactant in the continuous phase, Bel Fdhlia & Duineveld (1996) showed that the presence of surfactants has no effect on the bubble dynamics once the surfactants are concentrated in a small region close to the bubble rear. This was confirmed by Cuenot, Magnaudet & Spennato (1997) from direct numerical simulations. Concerning bubbles rising in water, several investigators (Aybers & Tapucu 1969*a*; Duineveld 1994) have observed that the effect of surfactants diminishes as bubble size increases. Beyond a certain bubble size, and provided the experiment duration is not too long, the behaviour of bubbles rising in tap water can be considered to be the same as bubbles in pure water. For bubbles larger than $d = 2.4$ mm, Lunde & Perkins (1998) showed that surfactant effects are negligible. Is it also the case for the tap water used here? Duineveld (1994) measured the mean rise velocity and path oscillation frequency of bubbles in ultra-purified-water, and found that: $\langle v_z \rangle = 0.292\,\mathrm{m\,s^{-1}}$ and $\omega = 40.2\,\mathrm{rad\,s^{-1}}$ for $d = 2.3$ mm and $\langle v_z \rangle = 0.294\,\mathrm{m\,s^{-1}}$, $\omega = 44.0\,\mathrm{rad\,s^{-1}}$ for $d = 2.68$ mm. Duineveld also measured the velocity magnitude for the smallest bubble: $V = 0.335\,\mathrm{m\,s^{-1}}$ for $d = 2.3$ mm. These values are in agreement with the present result: $0.29 \leqslant \langle v_z \rangle \leqslant 0.31\,\mathrm{m\,s^{-1}}$, $V = 0.325\,\mathrm{m\,s^{-1}}$ and $\omega = 39.4\,\mathrm{rad\,s^{-1}}$

for $d = 2.5$ mm. This agreement allows one to conclude that all the present results are representative of the behaviour of a rising bubble in a pure liquid. This will be confirmed later from the measurements of the continuous-phase velocity.

The present work is limited to a single bubble diameter ($d = 2.5$ mm, $We = 3.6$). The comparison with the other studies allows an assessment of the range of validity of the present results. First, the bubble diameter is large enough for path oscillations to be observed ($d \geqslant 1.82$ mm, $We \geqslant 3.3$) whilst the effect of impurities can be neglected (here, this is true for d larger than about 2.0 mm). Second, the diameter is small enough to avoid shape oscillations ($d \leqslant 3.5$ mm, $We \leqslant 4.2$). The present results are thus representative of the first regime of path oscillations of a clean bubble, from the onset of path oscillations up to the threshold of shape oscillations.[†] From the full three-dimensional detection of the bubble interface, the present work provides an accurate characterization of this regime. Our observations show that two unstable modes develop successively. The growth of the first one leads to a plane zigzag motion, whilst the growth of the second mode causes the zigzag to change into a helix. In the region under investigation here, the saturation of the second mode was never achieved. For greater elevations, Aybers & Tapucu (1969*a*) observed that the final trajectory was always a circular helix. Saffman (1956) showed that a perturbed plane zigzag could transform into a helix, while the reverse never happened. In the regime considered, the circular helix is therefore the only stable trajectory.

Finally, it is worth noting that, owing to the constant relative orientation and shape of the bubble, the wake instability is the only possible cause of the path oscillations observed here. The prediction of the bubble motion thus requires taking into account the interaction between the bubble and the unsteady wake.

4. Liquid-induced velocity

Now, the focus is on the liquid velocity induced by the bubble motion. We will consider the time recordings of the two components of the liquid velocity measured at the centre of the test section, 300 mm above the injection. Each velocity sample will be analysed by taking into account the instantaneous location and orientation of the bubble.

4.1. *Available results concerning the liquid velocity induced by a rising bubble*

Before presenting the experimental results, it is appropriate to review the available knowledge. The potential flow around an ellipsoidal bubble moving at constant speed provides a fundamental reference since the corresponding liquid-velocity field is known analytically (Batchelor 1967, p. 455). In this case, the velocity has fore–aft symmetry and the velocity magnitude decays as the reciprocal of the cube of the distance to the bubble. Moore (1963, 1965) used the classical boundary layer theory and concluded that the influence of the viscosity on the liquid flow field induced by a moving bubble scales as $Re^{-1/2}$. As a consequence, it is often asserted that the velocity induced by a clean spherical bubble is predicted well by potential theory for Reynolds numbers greater than a few hundred (Biesheuvel & van Wijngaarden 1984). From direct numerical simulations of the flow past an axisymmetric ellipsoidal bubble of fixed shape, Dandy & Leal (1986) showed that Moore's approach is not valid for a deformed bubble. The effect of interface curvature has to be taken into account since

---

[†] The first regime observed by Aybers & Tapucu (1969*a*), $1.34 \leqslant d \leqslant 2$ mm, was influenced by surfactants.

it may cause flow separation for certain Reynolds numbers and aspect ratios (β). Using a method similar to Dandy & Leal's, Blanco & Magnaudet (1995) confirmed and extended this result. In particular, they determined the region in the (Re, β)-plane in which a standing eddy exists behind the bubble. The case under consideration here belongs to this region.

There is some experimental evidence for the existence of a significant wake behind rising bubbles. Most of this evidence has been obtained from visualization techniques. By taking photographs of a bubble rising from a region of high dye concentration, Maxworthy (1967) was the first to observe the unsteady wake behind a large rocking bubble ($d \approx 17$ mm). Using solid tracers in the liquid phase, Lindt (1972) and Lindt & De Groot (1974) observed helical vortices in the wake of bubbles with oscillating paths in water–glycerol solutions of different concentrations. By using small hydrogen bubbles as tracers, Bhaga & Weber (1981) visualized both steady wakes with a standing eddy and open unsteady wakes behind rectilinear rising bubbles in different viscous liquids. Lunde & Perkins (1997) used a visualization technique similar to that of Maxworthy (1967) and provided a detailed description of the wake behind bubbles that followed helical, zigzag or rocking paths. Their results seem to indicate that helical paths are associated with the existence of two attached vortex filaments in the wake, though zigzag or rocking motions are related to the shedding of hairpin vortices. More recently, Brücker (1999) used particle image velocimetry (PIV) combined with high-speed video recordings to provide simultaneous measurements of the bubble shape and the liquid velocity around an air bubble rising in water. In this case, the bubble diameter ranged from 4 to 8 mm and thus belonged to the regime where shape oscillations exist and are coupled with path oscillations. Brüker confirmed and detailed the observations of Lunde & Perkins (1997): '[...] the zigzagging motion is coupled to a regular generation and discharge of alternate oppositely oriented hairpin-like vortex structures'; 'For spiralling bubbles [...] the wake consists of a twisted pair of streamwise vortex filaments which are wound in an helical path and are attached to the bubble base at an asymmetrical position'. The existence of a wake behind bubbles rising on oscillating paths is thus well-established. The relationship between the near-wake structure and the bubble trajectory is qualitatively understood. Nevertheless, as far as we know, the nature of the flow field in front of the bubble and the decay of the liquid velocity perturbation in the wake are yet to be investigated.

Far behind a rectilinear moving bubble, the liquid velocity may be assumed to be quasi-parallel. By using the boundary layer approximations in the wake and a momentum balance over a large volume around the bubble, one obtains the liquid velocity in the far wake (Batchelor 1967, p. 348):

$$u_z/V = \tfrac{1}{16} Re \beta^{2/3} C_d (R/z) \exp\{-\tfrac{1}{8} Re (r/R)^2 (R/z)\}, \tag{17}$$

where R is the bubble equivalent radius, r the distance to the axis of symmetry, and z the distance along the axis of symmetry. Here, the drag coefficient, C_d, is based on the major axis, a, of the ellipsoid and the hydrodynamic force, T, exerted on the bubble:

$$C_d = 2T/\left(\pi a^2 \rho V^2\right). \tag{18}$$

The major drawback of (17) is that the distance beyond which the approximation becomes valid in not known. To obtain a better theoretical base for comparison with the experimental results, axisymmetric DNS of the flow field around an ellipsoidal bubble of fixed shape moving at constant velocity have been performed. The present simulations are similar to those of Blanco & Magnaudet (1995) and were obtained using the same code. In the current simulations the computational domain was

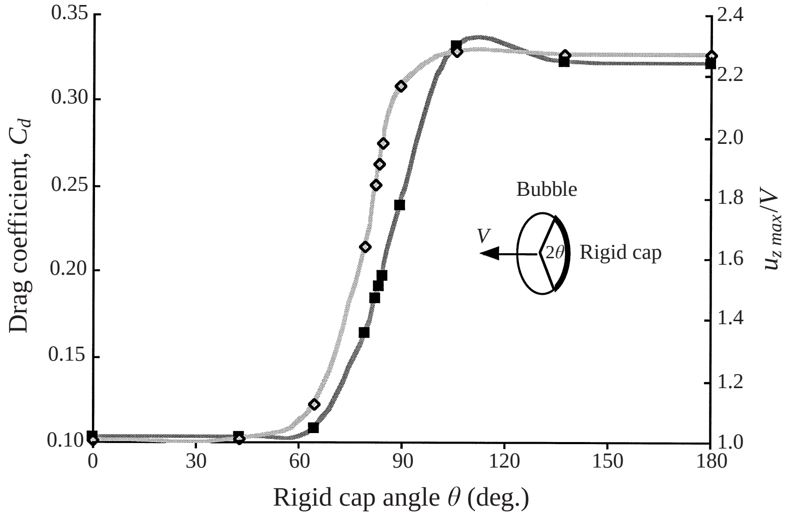

FIGURE 14. Drag coefficient and maximal liquid velocity of contaminated bubbles (from DNS): ■, G_d; ◇, $u_{z\,max}/V$.

extended to compute the far wake (up to $150R$) and the parameters were chosen to correspond to the present situation ($Re = 8 \times 10^2$, $\beta = 2.05$). The calculation was conducted in the frame of reference in which the bubble was fixed, with a constant and uniform velocity imposed far upstream and a free exit condition applied far downstream. After each simulation, the results were expressed in the laboratory frame where the bubble was considered to be moving at constant speed. The mesh grid was ellipsoidal and exactly followed the bubble shape. Furthermore, the mesh was refined in the boundary layer near the bubble (first mesh spacing of $0.0056R$) and on the symmetry axis in the wake (transversal mesh spacing from 0.00482 at the bubble rear to $0.055R$ at $150R$ behind). Several tests demonstrated that this mesh resolution allowed an accurate description of all the flow length scales. In order to investigate the possible influence of surface-active contaminants, different boundary conditions at the bubble surface were tested. The effect of the surfactants was modelled by the presence of a rigid cap which extended from the rear of the bubble up to the angle θ (figure 14). On the rigid cap region, a non-slip-velocity boundary condition was used whilst elsewhere a zero tangential shear-stress condition was imposed. The validity of this model was established by Cuenot *et al.* (1997) for slightly soluble surfactants by means of DNS of both the Navier–Stokes and surfactant-concentration equations.

Since the numerical code solves unsteady problems, the computations were started from a uniform velocity field. The present axisymmetric simulations always converged towards a stable steady solution. However, it must be remembered that this solution is unstable in real three-dimensional space and leads to oscillatory bubble motion. Consequently, the axisymmetric solution is not expected to exactly match the experiments. Nevertheless, it constitutes a useful reference case for making comparisons. Figure 14 shows the drag coefficient plotted against the rigid cap angle. It is evident that C_d varies from the value corresponding to a clean bubble ($\theta = 0$, $C_d = 0.103$) up to the value corresponding to a solid ellipsoid ($\theta = 180°$, $C_d = 0.322$). This variation is not smooth. For $\theta \leqslant 50°$, the departure from the clean bubble is negligible. For $50° < \theta < 120°$, C_d increases quickly whilst for $\theta \geqslant 120°$, the value of C_d is that of the rigid particle. For all θ, the flow behind the bubble is separated and a standing vortex

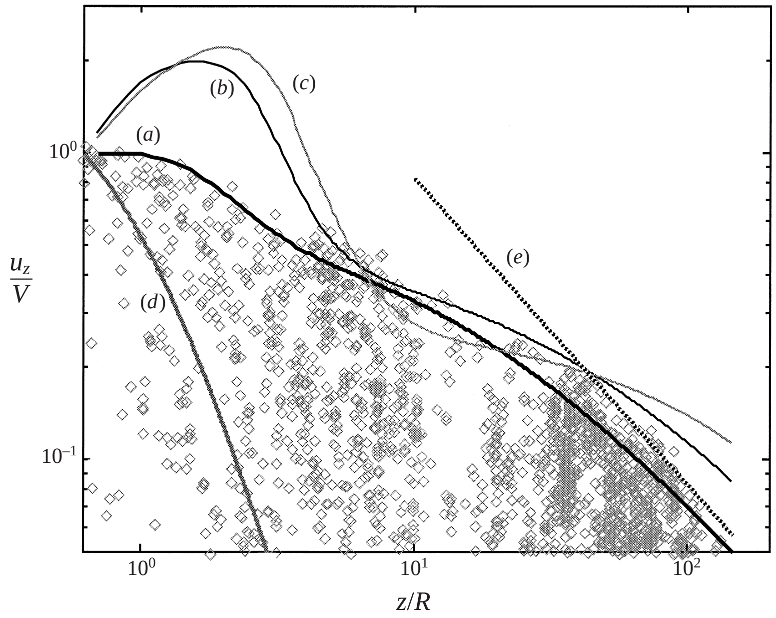

FIGURE 15. Decay of the vertical velocity on the symmetry axis behind the bubble: curve (*a*) DNS with $\theta = 0$ (clean bubble); (*b*) DNS with $\theta = 84°$ (partially contaminated bubble); (*c*) DNS with $\theta = 180°$ (rigid bubble); (*d*) potential flow theory; (*e*) far-wake theory (equation (17) with $C_d = 0.10$); ◇, measurements.

is present. Figure 14 also shows the maximal vertical liquid velocity, $u_{z\,max}$, which is due to the presence of the vortex. For a clean bubble $u_{z\,max}$ is equal to the bubble velocity while for a fully contaminated bubble it is 2.3 times greater. This maximal velocity may thus be used to detect the presence of surfactant effects.

By identifying the drag force, T, with the buoyancy in (18) and using experimental values of V and β, the experimental drag coefficient is obtained:

$$C_d = \tfrac{4}{3}(dg/V^2)\beta^{-2/3} \approx 0.2. \qquad (19)$$

This value is two times larger than the one predicted by the axisymmetric DNS for a clean bubble. One could suppose that such a discrepancy was due to the presence of surfactants (the experimental value is indeed obtained for $\theta = 84°$). However, there are arguments indicating that this explanation is not correct. In the first instance, for $\theta = 84°$, a maximum velocity approximately twice the bubble velocity should be detected in the liquid. From the results to be presented here (figures 15 and 20) it is shown that measured liquid velocities never exceeded 1.05 times the bubble velocity. Also, the experiments that were carried out by Duineveld (1994) in ultra-purified water led to the same bubble velocity as reported here. As claimed in § 3.3, the present bubble can be considered as *hydrodynamically clean.* The discrepancy between experiments and DNS is due to the fact that axisymmetric simulations provide unrealistic stable steady solutions. Our opinion is that the development of wake instabilities in real three-dimensional situations causes a significant increase of the drag coefficient. This hypothesis seems to be supported by numerical simulations. Esmaeeli, Ervin & Tyggvason (1993) showed two-dimensional simulations of bubbles in a periodic array and found that the rise velocity was sharply reduced when the bubbles started to wobble. Esmaeeli & Tryggvason (1999) also found that unsteady motion reduced the rise velocity of an array of bubbles, although in this case the unsteady motion resulted from the bubble interactions.

Figure 15 summarizes the theoretical results for the velocity field induced by an ellipsoidal bubble rising on a straight line. The vertical velocity on the symmetry axis is plotted against the distance behind the bubble. The potential flow result shows a rapid decrease of the velocity since it does not predict a wake (1% the bubble velocity at $5R$ behind the bubble). For a clean bubble, the DNS shows a long wake (5% of the bubble velocity at $145R$ behind the bubble). The predicted velocity tends towards the $1/z$ decay predicted by the far-wake theory; however the theory is not valid at $z = 150R$. For contaminated bubbles, DNS results exhibit a large overshoot of the velocity in the region just behind the bubble and a longer extension of the wake. Hereafter, we will compare the measurements with the potential flow prediction and the clean-bubble DNS. The far-wake theory will not be used since the region in which measurements were made was at the limit of the validity of this theory. The comparison between DNS of the region around a contaminated bubble and the measurements is shown in figure 15 (see § 4.4 for the description of the experimental results). These results confirm that the bubble is hydrodynamically clean.

4.2. *Liquid velocity close to the bubble* ($-10 \leqslant z \leqslant 10R$)

In the first instance, results for set A are considered. These measurements correspond to investigations up to a distance of about 10 radii from the bubble. Two components of the liquid velocity are measured at a fixed point located at 300 mm above the injection point. In this region the bubbles have reached their terminal velocity and their trajectory is represented well by a plane zigzag. Equations (1) and (3) give the bubble-centre coordinates relative to the LDA measurement point. Hereafter, the liquid velocity will be presented by setting the origin of the coordinates at the bubble-centre location.

Figure 16 gives the results of four typical experimental runs. The main graphs show the liquid velocity, u_z and u_y, versus the vertical distance to the bubble (positive z corresponds to velocity samples detected behind the bubble). The insets show the bubble trajectory relative to the measurement point. Comparisons with potential flow and DNS are shown. Since these theoretical velocity fields are known only for a bubble in translation, we proceed as follows. For each instant, the theoretical velocity fields are rotated in order to orient the z-axis parallel to the direction of the real bubble. Then, the predicted velocity at the point corresponding to the measuring volume is determined. This velocity is known for the potential flow field because it is determined analytically. However, for the DNS results the velocity at the measurement point is obtained by interpolation on the mesh grid. For both, the predicted velocities are arbitrarily set to zero whenever the bubble intersects the measurement point. The wavelength of path oscillations is approximately 50 mm and the bubble orientation changes by approximately 30° over a travel distance of $10R$. Since the predicted velocities correspond to a rectilinear moving bubble, these comparisons are relevant only for distances less than $5R$.

In the first example (figure 16*a*), the bubble axis is vertical at the instant the bubble centre coincides with the measurement point. In front of the bubble, the potential theory and the DNS match the experiments. The vertical velocity quickly increases from zero to V and the horizontal velocity is negligible since the measurement point is on the symmetry axis. Behind the bubble, the vertical velocity decreases from V to zero but the gradient is significantly smaller than that in front of the bubble. This fore–aft asymmetry due to the presence of a wake is ignored by the potential theory

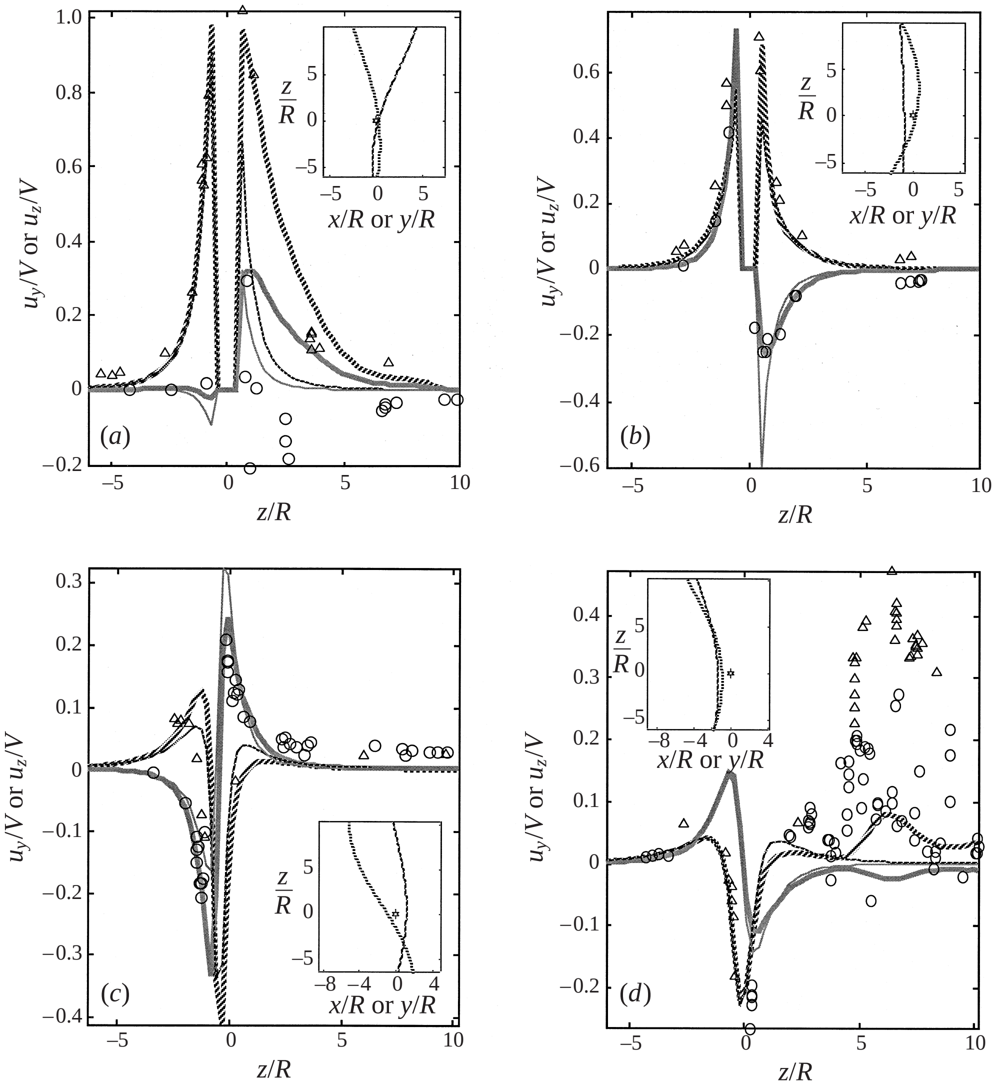

FIGURE 16. Liquid-velocity recordings from set A. Liquid velocity (main graph): △, u_z/V from measurements; ○, u_y/V from measurements; thick broken line: u_z/V from DNS; thick grey line: u_y/V from DNS; thin broken line: u_z/V from potential theory; thin grey line: u_y/V from potential theory. Insets: bubble trajectory: ✡, measurement point location, ——, $z(x)/R$, ······, $z(y)/R$.

but correctly predicted by DNS. Concerning the horizontal velocity, the negative values detected behind the bubble are predicted neither by the potential theory nor the DNS.

The second bubble (figure 16*b*) also intersects the measurement point, but its centre passes it at a horizontal distance of $0.9R$ and its axis is not vertical. In front of the bubble, the off-centring of the bubble axis causes decreased vertical velocities and increased horizontal velocities. Behind the bubble, the decrease of the vertical velocity is symmetric with the increase that is observed in front of the bubble. Negative horizontal velocities are also detected. These negative values are generated by the liquid that passes round the bubble to ensure conservation of the liquid volume.

Because of this particular bubble trajectory, the measuring volume is located outside the wake. Consequently, the potential theory provides a good approximation of the measurements although the DNS results remain slightly more accurate.

In the third example (figure 16*c*), the bubble does not intersect the measurement point. As in the preceding example, all the measurement points are located outside the wake. The measured velocities can thus be explained by the liquid displacement resulting from mass conservation and so the measurements, DNS and potential theory are in agreement.

The fourth example (figure 16*d*) represents another kind of trajectory for which the bubble orientation changes as it passes close to the measurement point. For $z < 2R$, since the measurement point lies outside the wake, potential theory and DNS predict the measurements well. For $z > 2R$, the change in the bubble orientation causes the wake to move across the measurement point. The vertical velocity increases to a maximum at $z = 7R$ and the horizontal velocity strongly fluctuates. The DNS predicts an increase of the vertical velocity behind the bubble, but considerably underestimates the intensity of the vertical and horizontal velocities. These discrepancies are taken to indicate an intense structure in the near wake of the bubble. This structure is detected while the bubble direction changes and has no equivalent in the axisymmetric DNS. It is probably a vortex generated at the bubble rear and related to the three-dimensional instabilities.

An analysis of the 81 experimental runs of set A revealed a different trajectory for each measurement. The comparison with the DNS and potential flow leads to the conclusion that two regions can be distinguished in the near flow field. In front of the bubble and far from its trajectory behind, the potential theory and DNS give the same results and match the experiments. (The DNS predictions are just slightly more accurate since they take into account the viscous effect in the boundary layer and the flow separation behind the bubble.) Behind the bubble an important wake is present. Depending on the exact region investigated, the DNS either provides correct predictions (figure 16*a–c*) or not (figure 16*d*). The near wake seems to be a combination of the steady wake predicted by the axisymmetric DNS and unsteady vortices that detach from the bubble rear.

By combining all the data provided by set A it is possible to reconstruct the velocity field around the bubble. The results of each velocity sample are transformed in the following way: (i) the measurement point is translated in order to place the bubble centre at the frame origin and (ii) the measured velocity is rotated in order to align the bubble axis with the z-axis. This second operation raises two difficulties. First, the LDA sampling times of the two velocity components do not coincide. Second, only two components of the bubble velocity are available. The first problem was addressed by ensuring that the two LDA signals coincided. This was achieved using linear interpolation (with a time step of 0.1 ms) to regularly resample the signals between any consecutive samples separated by less than 5 ms. After this operation only the velocity samples that were present on two signals with a time separation less than 0.1 ms were retained. The second problem was solved by assuming that the velocity field close to the bubble was axisymmetric. By assuming a zero azimuthal component it was possible to determine the two velocity components in the meridian plane that contained the bubble axis.

The reconstructed velocity field is shown in figure 17. In this figure only the region in which bubble orientation changes can be neglected is shown. The velocity is represented in the bubble frame. The upper part of the figure displays the measurements whilst the lower part shows the DNS results at the locations where experimental

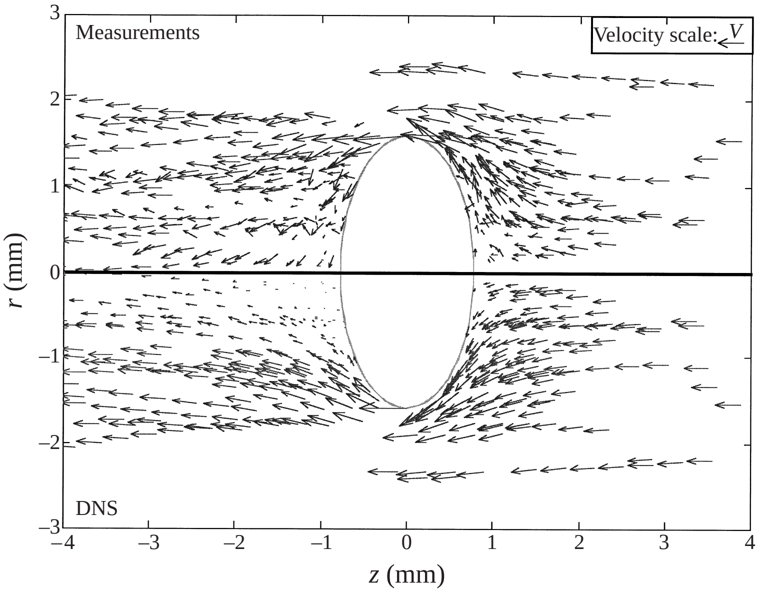

FIGURE 17. Near velocity field represented in the bubble frame. Upper part: results of the 81 experimental runs of set A; lower part: DNS predictions at the points where measurements are available.

samples are available. This representation confirms the existence of two regions. In the potential region, the measurements are in excellent agreement with the DNS (and the potential theory). In the wake, different velocities samples can be obtained at the same location. The flow there is neither axisymmetric nor steady due to the presence of unsteady wake vortices.

4.3. *Liquid velocity far from the bubble* ($z \leqslant 150$)

The far wake is now examined from the experimental results of set B. Figures 18 and 19 give two typical examples of liquid velocity recordings. The velocity is plotted versus the bubble elevation relative to the measurement point. In each figure we compare the results for two bubbles that have similar trajectories. The velocity of bubbles that have the same trajectory is similar (the small discrepancies observed are not significant owing to the slight differences in the trajectories). This was confirmed by five bubble pairs belonging to set B and one belonging to set A. This indicates that although the wake is not steady it remains deterministic.

For the examples selected, negligible velocities are measured close to $z = 0$ since the minimum distance between the bubble and measurement point is larger than $5R$. Significant velocities are nevertheless detected for z larger than $20R$. The vertical velocity (figures 18*b*–19*b*) is always positive, increasing from zero to a maximum and then decreasing smoothly back to zero. The horizontal velocity (figures 18*c*–19*c*) exhibits positive and negative values. These general trends are confirmed by the 47 runs of set B for which the vertical velocity always exhibits positive bump-shaped profiles (figures 18*b*–19*b*) whilst the horizontal velocity shows negative or positive bump-shaped profiles (figure 19*c*) or wavy profiles (figure 18*c*). The magnitude of the horizontal velocity is always significantly smaller than that of the vertical one.

The above results are interpreted as that, far from the bubble, a quasi-steady wake develops around the bubble-centre trajectory. The liquid velocity is parallel to the

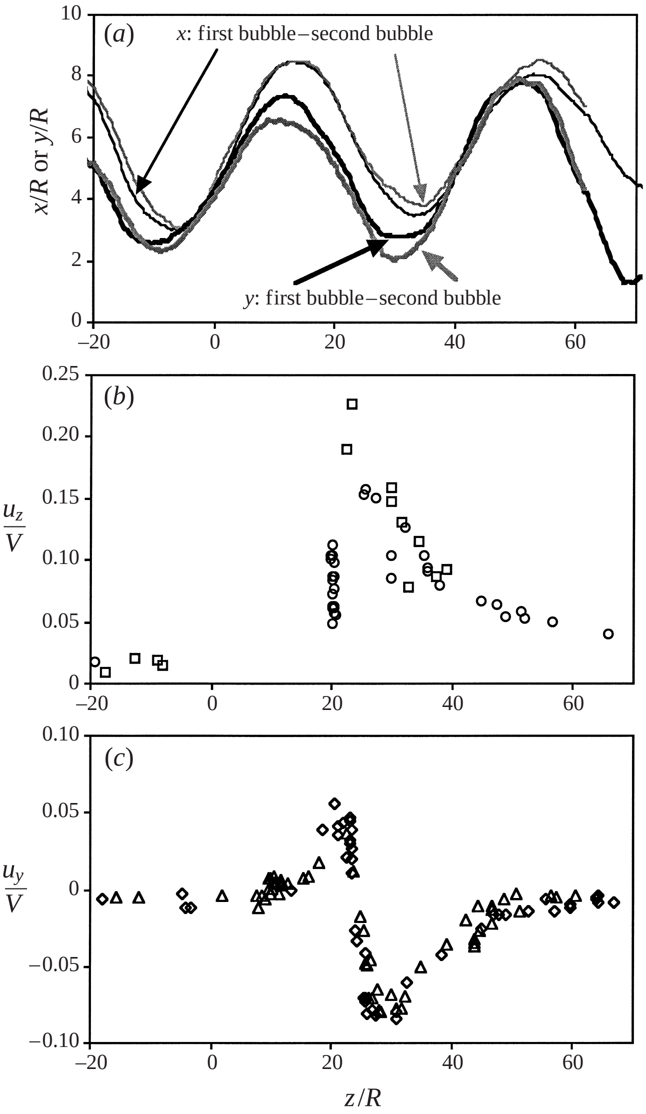

FIGURE 18. Liquid-velocity recordings far from the bubble: first example from set B. (*a*) Bubble trajectory. (*b*) Vertical velocity u_z/V: ○, first bubble; □, second bubble. (*c*) Horizontal velocity u_y/V: ◇, first bubble; △, second bubble.

bubble trajectory. Since the maximal trajectory inclination is 30°, vertical velocities are always positive and larger than the horizontal velocities. A positive vertical-velocity profile is detected at times for which the wake moves across the measurement point. On the other hand, the sign of the horizontal velocity depends on both the location of the measurement point and the local orientation of the wake.

4.4. *Decay of the liquid velocity with the distance from the bubble*

The previous interpretation implicitly assumes that the velocity induced by the wake vortices is small compared to that generated by the quasi-steady wake. It is useful to

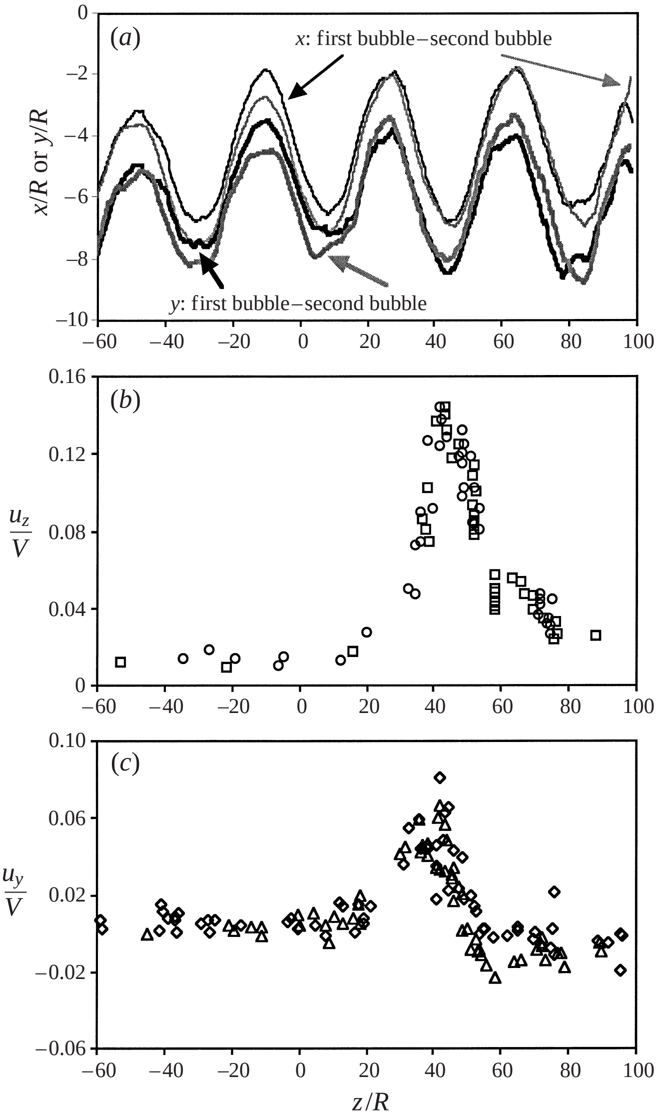

FIGURE 19. As figure 18 but for a second example from set B.

check this assumption by comparing the experimental decrease of the liquid velocity with the DNS prediction.

In figure 20, all the velocity measurements are plotted against the bubble elevation relative to the measurement point. Since the orientation of the bubble and its horizontal location are not taken into account, the results exhibit a considerable scatter. However, this scatter is not considered to be problem since the current focus is on the maximum velocity. To this end the maximal velocities predicted by DNS and potential theory are also represented in figure 20. For each z, we determined the maximal velocity predicted by the DNS (or potential theory) over all the possible bubble orientations (from 0 to 30° in steps of 1°). Note that, for z larger than $2R$, the largest DNS velocity magnitude is the velocity $u_{z\,max}$ computed on the symmetry axis.

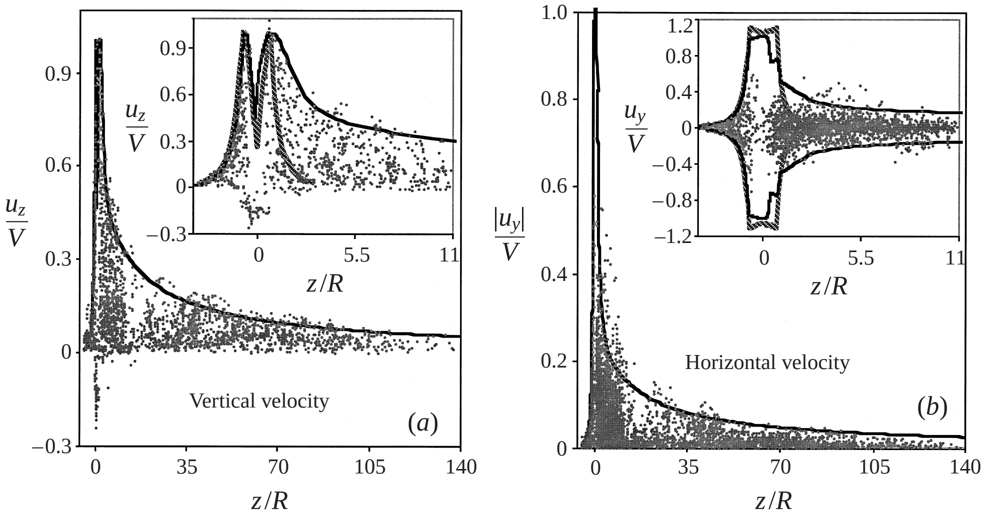

FIGURE 20. Velocity decay behind the bubble: thick line: maximal velocity from DNS; broken line: maximal velocity from potential theory; •, measurements.

The maximum vertical velocity is hence $u_{z\,max}$ and the maximal horizontal velocity is $u_{z\,max}$ multiplied by the sine of the maximum angle (30°).

In front of the bubble the liquid velocity is predicted well by both the potential theory and DNS. Behind the bubble, an intense and long wake develops (5% of the bubble velocity at a distance of $150R$ behind the bubble). The potential flow shows an unrealistic rapid decay. On the other hand, most of the velocity samples are located under the DNS maximum. Among the few measurements that exceed the DNS maximum, the largest overshoots are for the horizontal velocity in the near wake. The DNS thus provides a satisfactory prediction of the general decrease of the maximum velocity over the whole range of distances investigated. This is confirmed by the logarithmic representation in figure 15.

Since the bubble motion exhibits oscillations, the liquid velocity is neither steady nor axisymmetric. Despite this lack of symmetry, the decrease of the velocity in the bubble wake is predicted well by the axisymmetric DNS. The structure of the wake seems to be controlled by two mechanisms. The first generates a quasi-steady wake that spreads around the bubble-centre trajectory. Its contribution to the velocity field is predicted well by the steady flow computed by the axisymmetric DNS provided the local orientation of the wake is taken into account. The second mechanism is related to the wake instability: the axisymmetric solution is unstable and unsteady vortices are generated at the bubble rear. However, except in the near wake, these vortices do not significantly influence the decay of the wake.

5. Concluding remarks

The present work deals with isolated air bubbles rising in still water. Both the bubble and liquid motions were investigated and the influence of surfactants was proved to be negligible. Since the bubble equivalent diameter was fixed to 2.5 mm ($We = 3.6$, $Re = 8 \times 10^2$), the present results are characteristic of the regime existing between the onset of path oscillations ($d = 1.82$ mm, $We = 3.3$) and that of shape oscillations ($d = 3.5$ mm, $We = 4.2$). We observed that after the initial acceleration stage, the bubble starts oscillating on an almost plane zigzag. This plane trajectory then progressively transforms into a helix, which is the final stable trajectory. The current investigation focuses on the transition between the zigzag and helical paths.

The bubble shape is found to be similar to an oblate ellipsoid of constant shape. At each instant, the symmetry axis of the ellipsoid is parallel to the bubble velocity, and the velocity magnitude is constant. Two harmonic modes are involved in path oscillations. They correspond to horizontal oscillations of the bubble velocity in two perpendicular directions. They have the same frequency and are $\pi/2$ out of phase with each other. In the region under investigation ($215 \leqslant z \leqslant 490\,\mathrm{mm}$), the amplitude of the primary mode is saturated while the amplitude of the secondary mode was always observed to be increasing. Two slow motions are superimposed onto this two-mode oscillation. The first is a slow horizontal drift that causes the trajectory axis to be slightly inclined. The second is a slow rotation of the principal directions of oscillations. These phenomena are not reproducible and have no influence on the two-mode dynamics. Their combination with the second-mode growth leads to complex trajectories. The characteristics of the bubble motion cannot therefore be determined without a complete three-dimensional interface tracking.

The liquid velocity induced by the bubble motion is deterministic and characterized by two regions. In front of and next to the bubble, the flow is potential. Behind the bubble, an intense long wave develops. The flow in the wake includes two contributions due to a quasi-steady wake that spreads around the bubble trajectory and wake vortices that are generated at the bubble rear. These vortices were described in detail by Lunde & Perkins (1997) and Brücker (1999). They have a strong influence on the flow just behind the bubble and on the hydrodynamic force that acts on it. They are the origin of the bubble path oscillations that cause the increase of the drag coefficient ($C_d = 0.1$ for the steady flow induced by a rectilinear rising bubble, $C_d = 0.2$ here). Nevertheless, they do not induce large liquid velocities and their influence on the intermediate- and far-wake intensity is small. The velocity decay behind the bubble is predicted well by the axisymmetric wake around a rectilinear rising bubble provided the local orientation of the wake is taken parallel to the bubble trajectory.

The authors would like to thank C. Daniel and D. Legendre for their help with the numerical simulations. K.E. gratefully acknowledges support from the Research Council of Norway.

REFERENCES

AYBERS, N. M. & TAPUCU, A. 1969*a* The motion of gas bubbles rising through stagnant liquid. *Wärme- und Stoffübertragung* **2**, 118–128.

AYBERS, N. M. & TAPUCU, A. 1969*b* Studies on the drag and shape of gas bubbles rising through a stagnant liquid. *Wärme- und Stoffübertragung* **2**, 171–177.

BATCHELOR, G. K. 1967 *An Introduction to Fluid Dynamics*. Cambridge University Press.

BEL FDHLIA, R. & DUINEVELD, P. C. 1996 The effect of surfactants on the rise of a spherical bubble at high Reynolds and Peclet numbers. *Phys. Fluids* **8**, 310–312.

BHAGA, D. & WEBER, M. E. 1981 Bubbles in viscous liquids: shapes, wakes and velocities. *J. Fluid Mech.* **105**, 61–85.

BIESHEUVEL, A. & WIJNGAARDEN, L. VAN 1984 Two-phase flow equations for a dilute dispersion of gas bubbles in a liquid. *J. Fluid Mech.* **148**, 301–318.

BLANCO, A. 1995 Quelques aspects de l'écoulements d'un fluide visqueux autour déformable: une analyse par simulation directe. Thesis 1063, INP Toulouse, France.

Blanco, A. & Magnaudet, J. 1995 The structure of the axisymmetic high-Reynolds number flow around an ellipsoidal bubble of fixed shape. *Phys. Fluids* **7**, 1265–1274.

Brücker, C. 1999 Structure and dynamics of the wake of bubbles and its relevance for bubble interaction. *Phys. Fluids* **11**, 1781–1796.

Cuenot, B., Magnaudet, J. & Spennato, B. 1997 The effect of slightly soluble surfactants on the flow around a spherical bubble. *J. Fluid Mech.* **339**, 25–53.

Dandy, D. S. & Leal, L. G. 1986 Boundary separation from a smooth slip surface. *Phys. Fluids* **29**, 1360–1366.

Duineveld, P. C. 1994 Bouncing and coalescence of two bubbles in water. PhD thesis, University of Twente, Netherlands.

Duineveld, P. C. 1995 The rise velocity and shape of bubbles in pure water at high Reynolds number. *J. Fluid Mech.* **292**, 325–332.

Ellingsen, K. 1998 Hydrodynamique des écoulements pilotés par l'ascension de bulles d'air virevoltantes. Thesis 1474, INP Toulouse, France.

Ellingsen, K. & Risso, F. 1998 Measurements of the flow field induced by the motion of a single bubble. In *Proc. Third Intl Conf. on Multiphase Flow*, *Paper* 286. ICMF.

El Sawi, M. 1974 Distorted gas bubble at large Reynolds number. *J. Fluid Mech.* **62**, 163–183.

Esmaeeli, A., Ervin, E. A. & Tryggvason, G. 1993 Numerical simulations of rising bubbles. In *Proc. IUTAM Conf on Bubble Dynamics and Interfacial Phenomena, Birminham, UK*, 6–9 Sept.

Esmaeeli, A. & Tryggvason, G. 1999 Direct numerical simulations of bubbly flows. Part 2. Moderate Reynolds number array. *J. Fluid Mech.* **385**, 325–358.

Ford, B. & Loth, E. 1998 Forces on ellipsoidal bubbles in a turbulent shear layer. *Phys. Fluids* **10**, 178–188.

Haberman, W. L. & Morton, R. K. 1954 An experimental study of bubbles moving in liquid. *Trans ASCE* **387**, 227–252.

Hartunians, R. A. & Sears, W. R. 1957 On the instability of small gas bubbles moving uniformly in various liquids. *J. Fluid Mech.* **3**, 27–47.

Ho, C. S. 1983 Precision of digital vision systems. *IEEE Trans. Pattern Anal. Machine Intell.* **5**, 1065–1075.

Lindt, J. T. 1972 On the periodic nature of the drag on a rising bubble. *Chem. Engng Sci.* **27**, 1775–1781.

Lindt, J. T. & De Groot, G. F. 1974 The drag on a single bubble accompanied by a periodic wake. *Chem. Engng Sci.* **29**, 957–962.

Lunde, K. & Perkins, R. J. 1997 Observations on wake behind spheroidal bubbles and particles. *Proc. ASME Fluids Eng. Div. Summer Meeting*, *Vancouver*, *Canada*, *Paper*. 97-3530.

Lunde, K. & Perkins, R. J. 1998 Shape oscillations of rising bubbles. *Appl. Sci. Res.* **58**, 387–408.

Magnaudet, J. & Eames, I. 2000 The motion of high-Reynolds number bubbles in homogeneous flows. *Ann. Rev. Fluid Mech.* **32**, 659–708.

Maxworthy, T. 1967 A note on the existence of wakes behind large rising bubbles. *J. Fluid Mech.* **27**, 367–368.

Melville, W. K. 1983 Wave modulation and breakdown. *J. Fluid Mech.* **128**, 489–506.

Mercier, J., Lyrio, A. & Forslund, R. 1973 Three-dimensional study of the nonrectilinear trajectory of air bubbles rising in water. *Trans. ASME: J. Appl. Mech.* **40**, 650–654.

Miskis, M., Vanden-Broeck, J.-M. & Keller, B. 1981 Axisymmetric bubble or drop in a uniform flow. *J. Fluid Mech.* **108**, 89–100.

Moore, D. W. 1963 The boundary layer on a spherical gas bubble. *J. Fluid Mech.* **16**, 161–176.

Moore, D. W. 1965 The velocity of rise of distorted gas bubbles in a liquid a small viscosity. *J. Fluid Mech.* **23**, 749–766.

Risso, F. 1999 Experimental investigation of the motion of a bubble in a gradient of turbulence. *Phys. Fluids* **11**, 3567–3569.

Risso, F. 2000 The mechanisms of deformation and breakup of drops and bubbles. *Multiphase Sci. Tech.* **12**, 1–50.

Risso, F. & Fabre, J. 1998 Oscillations and breakup of a bubble immersed in a turbulent field. *J. Fluid Mech.* **372**, 323–355.

Ryskin, G. & Leal, L. G. 1984 Numerical solution of free-boundary problems in fluids mechanics.

Part 2. Buoyancy-driven motion of a gas bubble through a quiescent liquid. *J. Fluid Mech.* **148**, 19–35.

Saffman, P. G. 1956 On the rise of small air bubbles in water. *J. Fluid Mech.* **1**, 249–275.

Suzanne, C., Ellingsen, K., Risso, F. & Roig, V. 1998 Local measurements in turbulent bubbly flows. *Nucl. Engng Des.* **184**, 319–327.

Tsuge, H. & Hibino, S.-I. 1977 The onset conditions of oscillatory motion of single gas bubbles rising in various liquids. *J. Chem. Engng Japan* **10**, 66–68.